2012

Experimental Investigation of Transonic Shock Oscillations on NACA 0018 at Incidence

Christopher Allen Farrell

EXPERIMENTAL ANALYSIS OF TRANSONIC SHOCK OSCILLATIONS ON A NACA 0018 AT INCIDENCE

A Thesis
presented in partial fulfillment of requirements
for the degree of Master of Science
in the Department of Engineering Science
with an emphasis in Aeroacoustics
The University of Mississippi

by

CHRISTOPHER ALLEN FARRELL

August 2012

ABSTRACT

A NACA 0018 airfoil model with a 3-inch chord was mounted into the trisonic wind tunnel at the National Center for Physical Acoustics at the University of Mississippi. Tunnel runs were conducted with the angle of incidence increasing from 0° to 6° at 1° increments, while the Mach number was held steady at 0.73. High-speed schlieren images were recorded at a sample rate of 4,000 Hz. A Matlab code was developed to display the spatial power spectral density distribution in the region of the shock. This code calculated the frequency spectrum at regular points along the range of shock motion and plotted the spatial distribution of frequency spectra across all the points. This identified the location of the high-amplitude frequencies, which indicated the precise range of the shock motion as well as its dominant oscillation frequency. It was found that, for each degree increase, the frequency of oscillations increased by approximately 10.8 Hz. This is equivalent to a reduced frequency increase of 0.0205 per degree.

ACKNOWLEDGMENTS

I would like to thank Dr. Nathan Murray for his mentorship throughout this degree program, and Bernard Jansen for his guidance and input. I would also like to recognize the faculty of the National Center for Physical Acoustics, as well as a fellow student, Greg Lyons, for their support. Finally, I would like to thank my wife, Rachel Farrell, for her editorial assistance.

TABLE OF CONTENTS

LIST OF FIGURES

CHAPTER 1
INTRODUCTION

Buffeting is a phenomenon that arises from an unsteady pressure field, and the source of the unsteady pressures may be either external or internal to the local flow field. When buffeting is encountered, it can cause such undesired effects as loss of lift, control instability, and structural failure, and in the worst cases, the ramifications can be catastrophic. The study of buffeting has been developing for the last eighty years after it was determined to be responsible for the Meopham disaster in the 1930s, but the investigations that stemmed from that incident were mainly focused on how unsteady pressures external to a local flow field, such as gusting and wake turbulence shedding off of an aircraft's wing, could affect the tail wing (Spooner, 1931).

Precursory research into buffeting resulting from unsteady pressures internal to the local flow field, such as self-sustained shock oscillations, began in the early 1950s with experiments such as Hilton & Fowler (1952), Sorenson *et al.* (1951), and Humphreys (1951), but the field of study did not fully begin to take off until after the invention of the supercritical airfoil, when aircrafts began routinely operating within the transonic domain. Modern buffeting research now has practical applications that pertain to many aerodynamic technologies such as aileron buzz, blade cascades, helicopter rotor noise, helicopter VNE, supersonic intakes, and wing flutter.

A comprehensive buffeting model that accurately predicts buffeting onset and behavior has proven elusive. The contemporary theory of buffeting is based on the interaction between a transonic shock and boundary layer separation. As the boundary layer over the rear of an airfoil separates and grows larger, it alters the pressure on the downstream side of the

transonic shock, which in turn causes the shock to shift its position in accommodation to the modified pressure field. When boundary layer separation is induced by a transonic shock, the situation can become more complicated because it may establish a recursive interaction that produces a sort of dance between the shock and the boundary layer as each one cyclically affects the other. This concept is depicted in Fig. 1.1. A more detailed discussion of shock-induced separation (SIS) and shock/boundary layer interactions (SBLI) is covered in Sections 1.2 and 1.3.

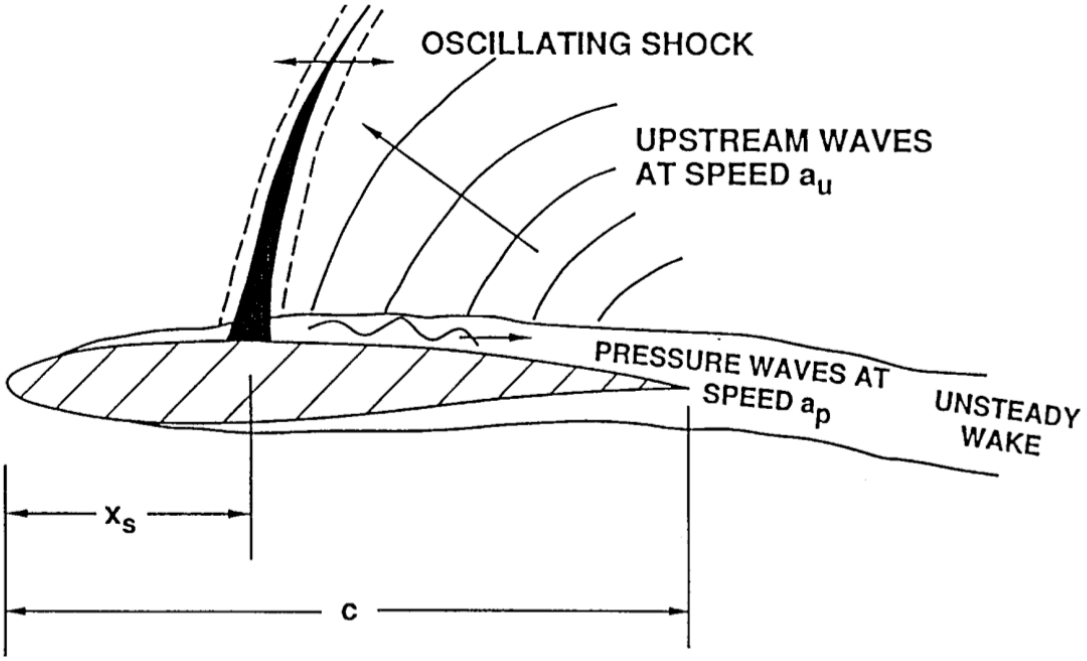

Figure 1.1. Visualization of Self-Sustaining Buffeting Theory (Lee, 2001)

Computational fluid dynamics (CFD) has been demonstrated to be a valuable aid for studying buffeting, but numerical buffeting models are still a work in progress. Computational research on buffeting began in the 1970s, but during that time numerical models (Rubesin *et al.*, 1976; Deiwert *et al.*, 1976; Wilmoth, 1977; Levy, 1978; Marvin *et al.*, 1980; Pulliam & Steger, 1980; Mercer *et al.*, 1981) were largely concerned with validating results against experimental data for future use. Transonic flows are fraught with nonlinearities

and are therefore inherently difficult to model and resolve, so throughout the rest of the twentieth century, studies (Ricketts, 1983; Lee, 1984; Williams *et al.*, 1985; Drela, 1986; Brentner *et al.*, 1997; Edwards, 1996; Prananta, 1999; Barakos & Drikakis, 2000) focused on refining computation schemes to improve accuracy and efficiency. These efforts achieved modest successes but were often only reliable for the particular cases being tested. Since the turn of the millennium, computation schemes have continued to improve and expand their applicability, but they have not yet reached the level of practicality required for full-scale use. In recent history, computational studies (Thomas *et al.*, 2002; Djavareshkian & Islami, 2004; Morgans *et al.*, 2003; Xiao *et al.*, 2006; Chen *et al.*, 2010; Raveh & Dowell, 2011; Xiong *et al.*, 2010; Ngoc & Hung, 2011) have still been focused on increasing accuracy and efficiency as in the past, but the results have begun to produce insightful details about the mechanisms of buffeting, which will be discussed further in Sections 1.2 and 1.3.

Though strides have been made in CFD modeling of buffeting over the last 40 years, codes can be very time-intensive to resolve and are generally valid for only a narrow range of flow conditions. Furthermore, as long as the mechanisms and pathways contributing to buffeting remain in question, CFD codes will continue to need revision. Therefore, there is still a need for additional experimental data for use in verifying computational results and further developing a comprehensive model of buffeting. The present study aims to contribute to the understanding of buffeting by examining the effects that the angle of incidence of an airfoil has on transonic shock oscillations.

1.1 Compressibility Effects on an Airfoil

Transonic flow refers to a flow field that exhibits both subsonic and supersonic velocities simultaneously. Transonic conditions are generally expected to manifest when the freestream Mach number ranges from 0.8 to 1.2, but this range is only approximate. The actual freestream Mach number that will result in a transonic flow varies with the geometry of the flow disturbance, which will be the shape of a given airfoil, for the purpose of this discussion.

When an airfoil is placed into a subsonic flow, there will be local velocities near the airfoil that will exceed the mean flow velocity and will rise as the freestream Mach number rises. For a given airfoil, there exists a freestream Mach number, known as the critical Mach number, for which the local velocity at a point on the airfoil will becomes sonic. Subsection 1.1.1 through Subsection 1.1.4 is a theoretical review, summarized from the work by Anderson (2001), on how a flow reaches the critical Mach number for a given airfoil.

1.1.1 Subsonic Compressible Flow Transition

All flows are compressible, but there are circumstances where it is reasonable to assume that the compressibility effects are negligible and may be ignored. A general rule of thumb for when compressibility effects should be considered is when the Mach number of a flow exceeds 0.3. This can be demonstrated by examining Euler's equation:

$$dp = \rho \, V dV. \tag{1.1}$$

By multiplying the right side of the equation by 1 in the form of $\frac{V}{V}$ and then dividing both sides of the equation by p, Euler's equation may be written as

$$\frac{dp}{p} = \frac{\rho}{p} \, V^2 \frac{dV}{V}. \tag{1.2}$$

If the equation is considered to be incompressible (denoted by ρ_0), it can be written as

$$\left(\frac{dp}{p}\right)_{\rho_o} = \frac{\rho_0}{p} \, V^2 \frac{dV}{V}. \tag{1.3}$$

Now by dividing equation 1.2 by equation 1.3, the expression

$$\frac{dp/p}{(dp/p)_{\rho_o}} = \frac{\rho}{\rho_0} \tag{1.4}$$

is obtained, and it conveys how density will vary from stagnation conditions for a given velocity differential.

This can be further illustrated by plotting the isentropic relationship that the density ratio has to the Mach number of a flow:

$$\frac{\rho}{\rho_0} = \left(1 + \frac{\gamma - 1}{2} M^2\right)^{1/\gamma - 1}. \tag{1.5}$$

Fig. 1.2 shows how the density of air varies with Mach number. At 0.3, the density has varied nearly 5% from the stagnation condition. Generally in an integrated flow field this has little effect on the accuracy of calculating other flow parameters, but as the Mach number continues to rise, the variations in density will begin to skew the calculations of other parameters too severely; this is when compressibility effects must begin to be considered.

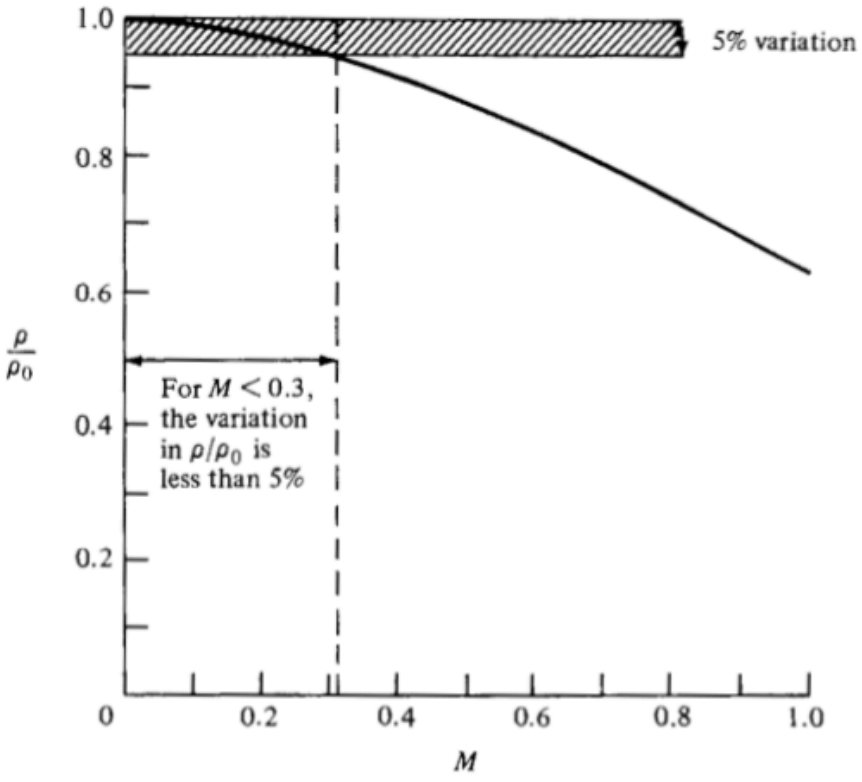

Figure 1.2. Density Variation with Mach Number (Anderson, 2001)

1.1.2 Coefficient of Pressure

The coefficient of pressure is a nondimensionalized metric defined by

$$C_p \equiv \frac{p - p_\infty}{q_\infty}. \tag{1.6}$$

It relates a local surface pressure (p) on a disturbance in a flow field to the freestream pressure (p_∞) of the flow field. This is a common metric used in discussions of airfoils, but the coefficient of pressure is only valid for low-speed, incompressible flows.

1.1.3 Compressibility Correction

Once compressibility effects become significant, a correction must be applied to the coefficient of pressure. The first correction that was developed to address this issue was the Prandtl-Glauert rule. It was formulated through inspection of the linearized velocity potential with the assumption of small perturbations. The correction uses the Mach angle β, which is defined by

$$\beta \equiv \sqrt{1 - M_\infty^2}, \tag{1.7}$$

to adjust the incompressible coefficient of pressure. The corrected compressible coefficient of pressure then takes the form

$$C_p = \frac{C_{p,0}}{\beta}, \tag{1.8}$$

where $C_{p,0}$ is the incompressible coefficient of pressure.

The Prandtl-Glauert rule was a significant improvement in assessing the coefficient of pressure for higher speed subsonic flows, but since it was based on a linearized assumption, it was still not as effective as could be desired. This led to further attempts at formulating a compressibility correction that accounted for nonlinearities. One improvement attempt that was utilized during World War II was the Karman-Tsien rule, which is calculated by

$$C_p = \frac{C_{p,0}}{\beta + (M_\infty^2/1 + \beta)C_{p,0}/2}, \tag{1.9}$$

and another more recent attempt is the Laitone rule, which is calculated by

$$C_p = \frac{C_{p,0}}{\beta + (M_\infty^2[1 + ([\gamma - 1]/2)M_\infty^2]/2\beta)C_{p,0}}. \tag{1.10}$$

1.1.4 Critical Mach Number

Now that the issue of correcting the coefficient of pressure for the compressibility is handled, the matter of calculating the critical Mach number for an airfoil can be addressed. Begin by allowing p_A to represent the pressure at point A on an airfoil. Then, by applying the isentropic relationship for stagnation pressure and flow field pressure conditions, the ratio of pressure at point A and the freestream pressure can be written as

$$\frac{p_A}{p_\infty} = \frac{p_A/p_0}{(p_\infty/p_0)} = \left(\frac{1 + [(\gamma - 1)/2]M_\infty^2}{1 + [(\gamma - 1)/2]M_A^2}\right)^{\gamma/(\gamma-1)}. \tag{1.11}$$

By utilizing an alternate form of the coefficient of pressure that is written as

$$C_{p,A} = \frac{2}{\gamma M_\infty^2}\left(\frac{p_A}{p_\infty} - 1\right), \tag{1.12}$$

the ratio of p_A/p_∞ can be replaced by the relationship in equation 1.11 to acquire the coefficient of pressure in the form:

$$C_{p,A} = \frac{2}{\gamma M_\infty^2}\left[\left(\frac{1 + [(\gamma - 1)/2]M_\infty^2}{1 + [(\gamma - 1)/2]M_A^2}\right)^{\gamma/(\gamma-1)} - 1\right]. \tag{1.13}$$

To find the critical Mach number, set M_A^2 equal to sonic conditions so that $C_{p,Cr}$ is now

$$C_{p,Cr} = \frac{2}{\gamma M_{Cr}^2}\left[\left(\frac{1 + [(\gamma - 1)/2]M_{Cr}^2}{1 + (\gamma - 1)/2}\right)^{\gamma/(\gamma-1)} - 1\right]. \tag{1.14}$$

Then set $C_{p,Cr}$ equal to one of the equations from Section 1.1.3, and set $C_{p,0}$ equal to the lowest incompressible value for the coefficient of pressure for a given airfoil. The freestream

Mach number that solves the equation will be the critical Mach number for that airfoil.

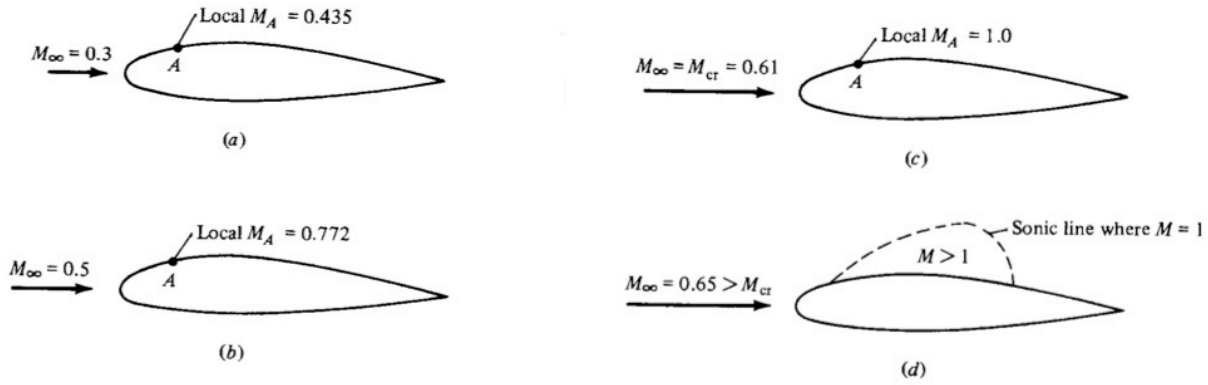

Figure 1.3. Development of Transonic Flow (Anderson, 2001)

1.2 Shock-Induced Separation

Once the freestream Mach number reaches the critical Mach number for an airfoil, any further increase in the freestream velocity will result in a localized region of supersonic flow developing on the airfoil. A principal feature of transonic flow is the shock that separates the transition between the regions of supersonic and subsonic flow. The position of the transonic shock is determined by the pressure gradient across the surface of an airfoil, and the surface pressure gradient is a function of the entire flow field around the airfoil. Increasing the freestream Mach number beyond the critical Mach number will eventually result in SIS and can eventually give rise to transonic shock oscillations and buffeting.

The parameters that affect self-sustained shock oscillations are the freestream Mach number, Reynolds number, angle of incidence, and airfoil geometry, but the crux of the theory of buffeting lies in the interaction between a shock and boundary layer separation. Therefore, before further discussing the details of self-sustained shock oscillations and buffeting, an understanding is required of how boundary layer separation occurs and behaves on airfoils at transonic speeds. A series of studies on SIS were performed by Pearcey et al. and culminated into the classical work "The interaction between local effects at the shock and rear separation - a source of significant scale effects in wind-tunnel tests on aerofoils and wings,"

published in 1968. The current author was able to obtain two preliminary studies on SIS by Pearcey (Pearcey, 1959; Pearcey & Holder, 1967), but the classical study was not available. This was not a problem, though, because an in-depth overview of the classical study can be found in a number of reports which were reviewed by the current author (Delery *et al.*, 1986; Kim *et al.*, 1993; Lee, 2001).

In the classical work by Pearcey et al., two primary types of SIS are identified and dubbed Type A and Type B. These two types of separation are depicted in Fig. 1.4. Type A separation, also known as "bubble separation" since its cross-section resembles a bubble, begins at the base of a transonic shock and extends toward the rear of the airfoil. It originates as the laminar boundary layer on an airfoil passes through the foot of the transonic shock, and the steep pressure increase creates an adverse pressure gradient which induces separation. Depending on the local flow field, the separation region may or may not reattach to the airfoil prior to reaching the tail edge. When the separation bubble fails to reattach, a large pressure divergence occurs at the trailing edge of the airfoil. The impact of this pressure divergence is discussed further in Section 1.2.3.

Type B separation, also known as "trailing edge separation," begins at the tail end of an airfoil and extends toward the transonic shock. Trailing edge separation is more common on supercritical airfoils than on conventional airfoils. This is because the asymmetrical shape of supercritical airfoils results in a strong pressure gradient on the rear curved portion of the airfoil. The pressure gradient steepens as the freestream Mach number rises and eventually reaches a point that induces a rapid growth of the boundary layer. If bubble separation is also present, a complex interaction may occur between the two regions of separation as they collide and combine together. Various permutations of the possible interactions between Type A and B separation are illustrated in Fig. 1.5. Further discussion of the nature of these interactions is beyond the scope of this thesis.

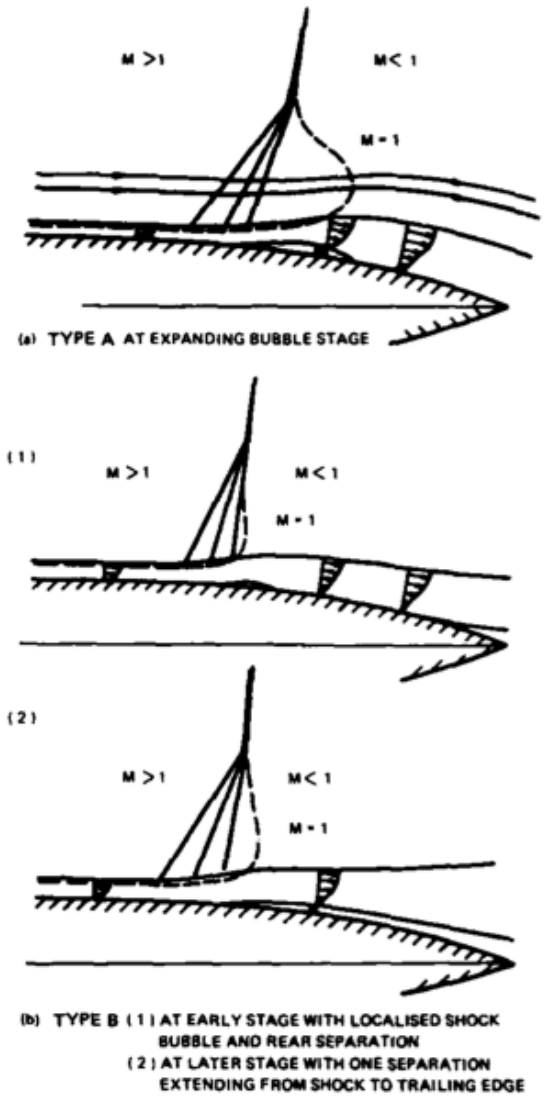

Figure 1.4. Depiction of Type A and Type B Separation (Elsenaar *et al.*, 1988)

1.2.1 Airfoil Geometry

Airfoil geometries can cause notable variations in the onset and behavior of boundary layer separation. In a study on trailing edge separation, Cunningham & Spragle (1987) found the shape of an airfoil to be the most significant factor affecting separation. Therefore, it is useful to review the different types of airfoils that commonly encounter transonic conditions. Various surveys of airfoil history and evolution were reviewed by the current author (Becker, 1980; Harris, 1990; Nelson & Zingg, 2004; Mason, 2006). The two fundamental types of

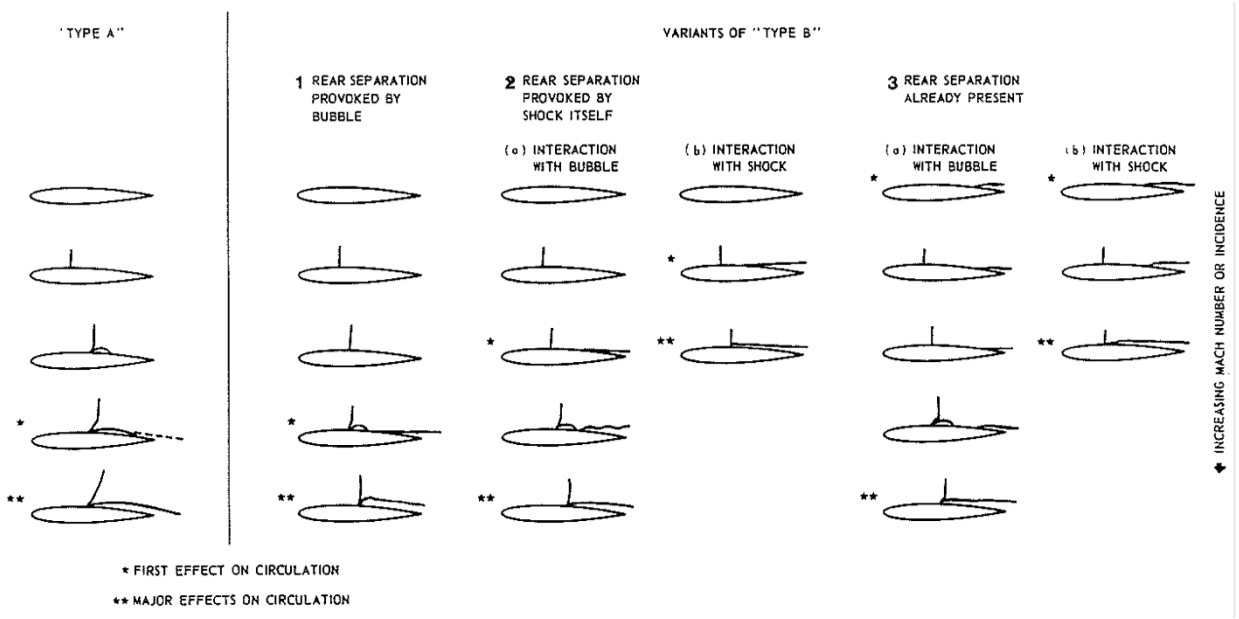

Figure 1.5. Various Permutations of Type A and B Separation Interactions (Tijdeman, 1977)

airfoils used for operating within the subsonic domain are conventional and supercritical airfoils. Conventional airfoils, such as the NACA family of airfoils, were the first type to be created. These airfoils perform well during subsonic flight, but their performance tends to wane in transonic conditions. The performance losses are due to a rapid increase in drag divergence, which manifests as losses in efficiency and lift.

Supercritical airfoils were developed to address the issue of drag divergence. The first attempt at creating supercritical airfoils was the Peaky airfoil, designed by Pearcey, where a supersonic region of flow was intentionally induced on the front of the airfoil. This effect was empirically found to reduce wave drag. However, the Peaky design was soon overshadowed by the invention of the Whitcomb airfoil, which set the stage for modern supercritical airfoil designs. The Whitcomb design utilizes a primarily flat upper surface for approximately the front two thirds of the airfoil chord and then slopes downward toward the trailing edge. The flat upper surface reduces the tendency of the flow to slow down as it crosses the surface of the airfoil, which in turn causes a reduction in the strength of the transonic shock. This effect is depicted in Fig. 1.6. This may have negligible effect on altering the critical Mach

number, but it decreases the freestream Mach number at which drag divergence occurs. This allows the supercritical airfoil to move through a faster flow field without suffering such severe performance losses as a conventional airfoil would.

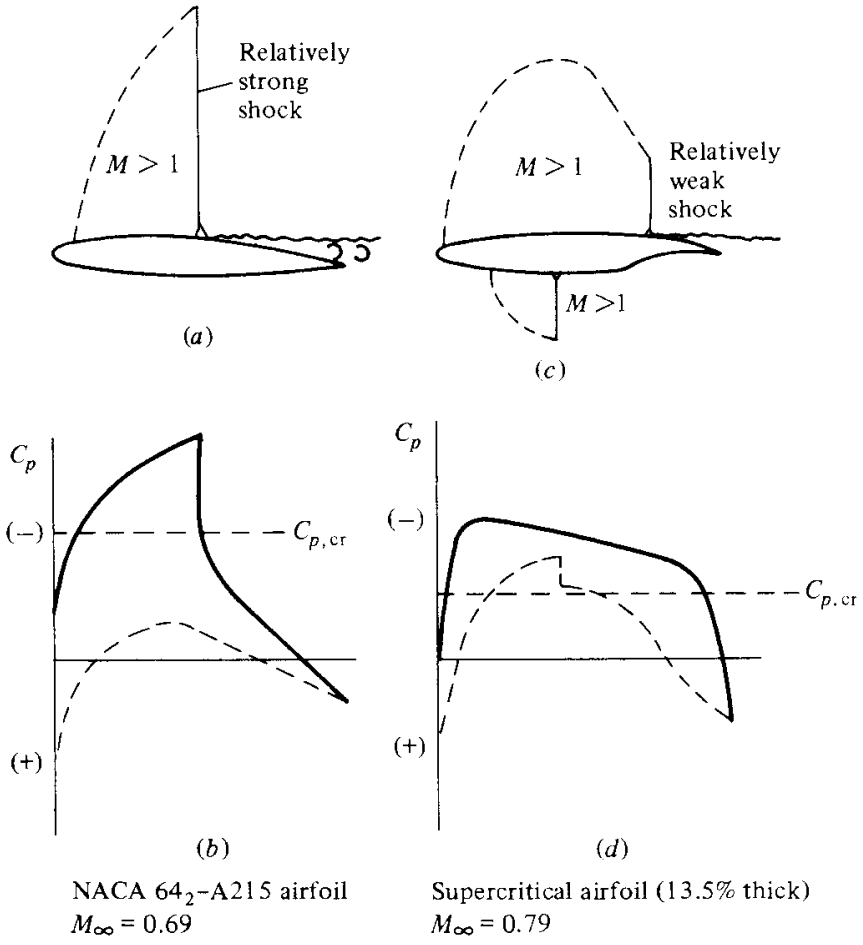

Figure 1.6. Weakening of Shock on Supercritical Airfoil (Anderson, 2001)

One other type of airfoil that is commonly studied in buffeting research is the biconvex airfoil. This airfoil is designed for supersonic flight, not transonic, but in order to reach supersonic speeds, it must pass through the transonic domain. Therefore, the characteristics of buffeting it exhibits at transonic speeds are still of interest.

1.2.2 Role of the Reynolds Number

The effect of Reynolds number on SIS has varying effects depending on the aspect of separation being examined. The onset of Type B separation is a direct result of Reynolds number effects due to the nature of that phenomenon, but the onset of Type A separation has been found to be weakly dependent upon Reynolds number and instead primarily dependent upon shock strength. The pressure ratio that has been determined to induce incipient separation is when p_2/p_1 reaches 1.4 (equivalent to a Mach number upstream of the shock of 1.16), but at this pressure ratio the separation will not be pronounced enough to have a noticeable effect. The point at which separation becomes appreciable is when the p_2/p_1 reaches 1.8 (equivalent to a Mach number upstream of the shock of 1.3). Once separation has occurred, the effect of the Reynolds number becomes more substantial because it plays a role in whether or not bubble separation remains attached (Elsenaar *et al.*, 1988).

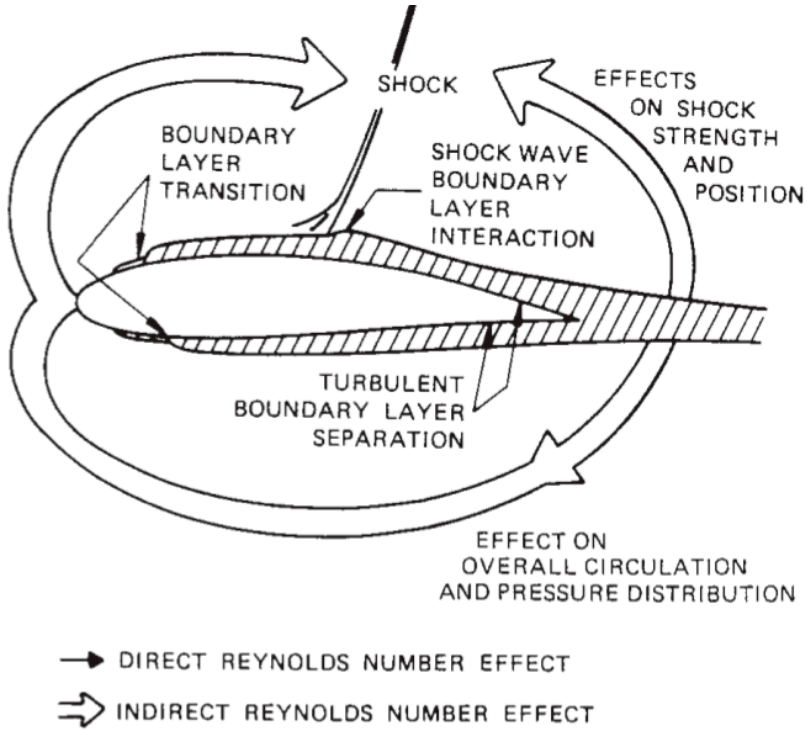

Figure 1.7. Effects of Reynolds Number on Flow Field (Elsenaar *et al.*, 1988)

1.2.3 Shock/Boundary Layer Interaction

Boundary layer separation can be thought of as analogous to an angled flap on the rear of a airfoil. In the classical study on shock motion, Tijdeman (1977) installed a tail flap that could be adjusted to various angles onto a NACA 64A006. A range of flap angles were tested while the freestream Mach number was held static at a speed capable of producing transonic flow. The tail flap angle was found to have a significant influence on the position of the shock. This is due to the compression and expansion effects that the flap induces in the overall flow field. The effect that the tail flap angle had on the shock position is shown in Fig. 1.8.

Tijdeman also studied the effects of an oscillating tail flap and found that the shock motion correlated to the flap motion. This implies that pressure perturbations propagating upstream from the tail flap are responsible for shock motion. Tijdeman dubbed these upstream propagating waves "kutta waves" because the propagating waves were assumed to be formed as a response of the pressure field attempting to satisfy the kutta condition at the tail edge of the airfoil. The kutta condition states that a wake cannot support a pressure differential, so the flow field must adjust the pressure field around an airfoil such that the pressures on the top and bottom side of the wake will be equal downstream of the airfoil. Johnson & Bachalo (1980) showed this condition to be valid for mild angles of incidence, and Johnson *et al.* (1981) later showed the kutta condition to even be valid for very severe angles of incidence. An illustration of propagating kutta waves can be seen in Fig. 1.9.

To further explore the source of unsteady pressure fluctuations in transonic flows, Benard *et al.* (2010) performed a wind tunnel experiment with a circular arc-shaped bump mounted on the tunnel wall. Shock motion was correlated to the upstream and downstream conditions. There was little to no unsteadiness found in the upstream conditions, and it was concluded that the pressure perturbations causing the shock motion did not come from upstream. However, a high correlation was found between the frequency of the shock motion and the frequency of pressure fluctuations at the reattachment point in the separated

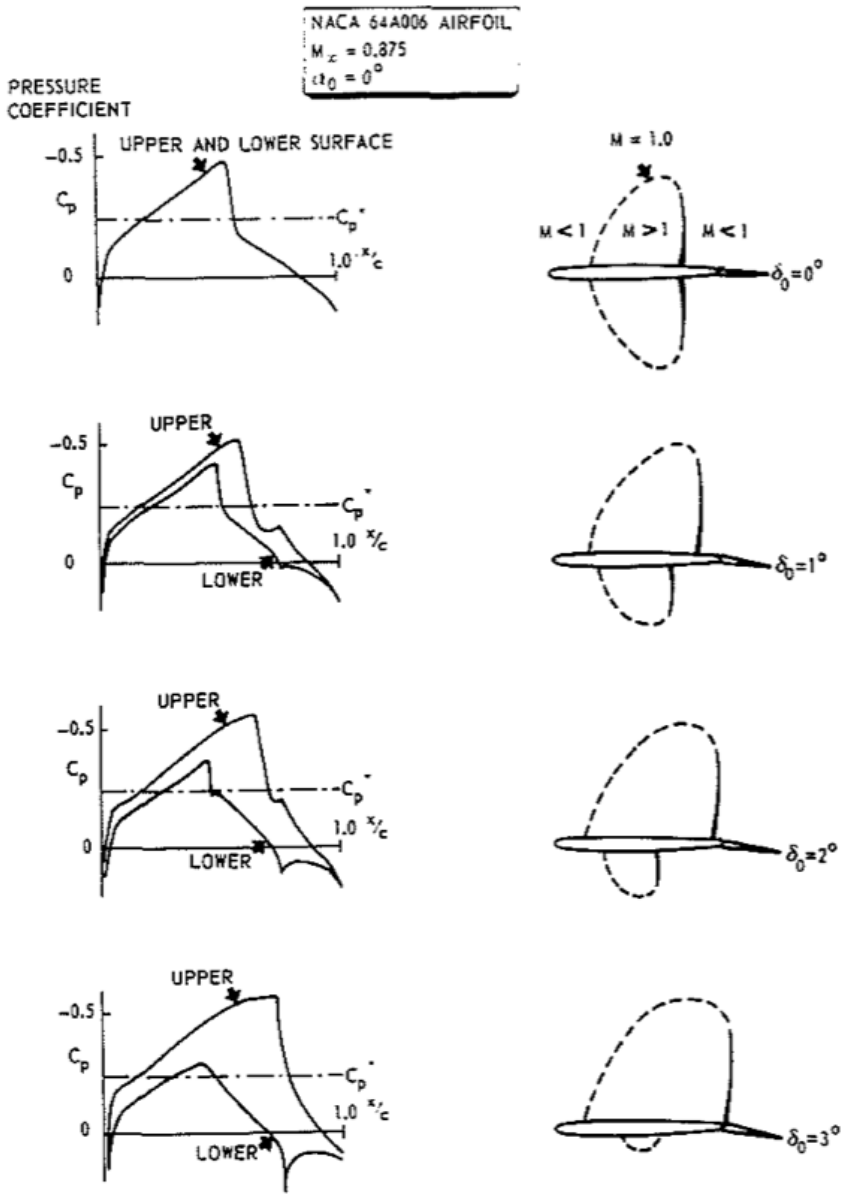

Figure 1.8. Effect of Tail Flap Angle on Shock Position (Tijdeman, 1977)

region downstream. This result is in agreement with the findings of other studies on SBLI performed by Dupont *et al.* (2006), Dussauge & Piponniau (2008), and Hartmann *et al.* (2012), and suggests that pressure fluctuations responsible for shock motion originate in the wake downstream.

In an early study on shock motion, Humphreys (1951) found that at high speeds, as the angle of incidence of the airfoil increases, the amplitude of pressure pulsations on the surface

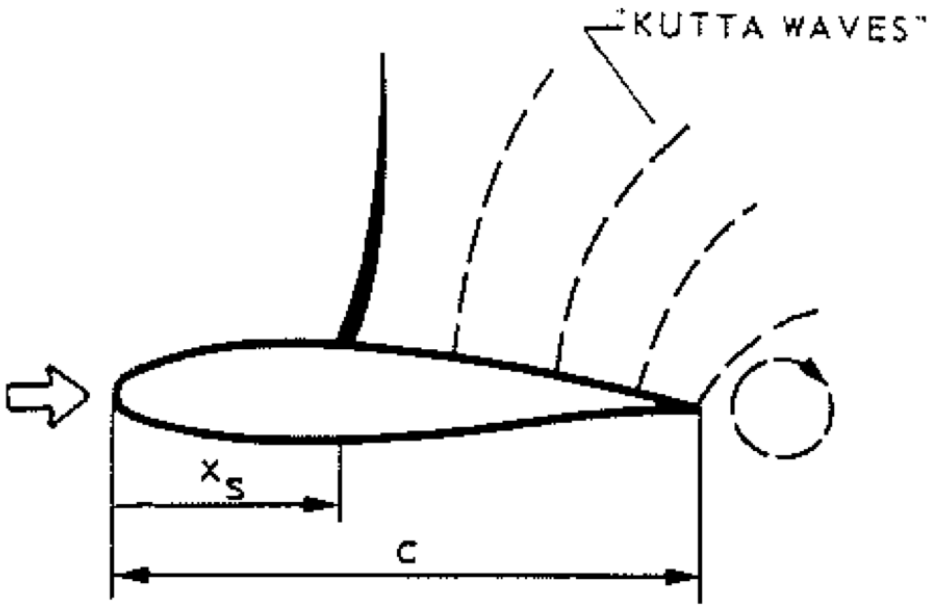

Figure 1.9. Illustration of Kutta Wave Theory (Tijdeman, 1977)

of the airfoil also increase. Pearcey (1959) explained that this phenomenon stems from increased separation at the trailing edge resulting from the combination of the separation induced by Mach number and the separation induced by angle of incidence. Since the pressure recovery is attempting to satisfy the kutta condition, this larger separated region at the trailing edge creates larger pressure pulsations.

1.3 Periodic Shock Motion

Self-sustained shock oscillations are a product of SBLI. When a transonic shock induces boundary layer separation, it alters the pressure behind the transonic shock. This causes the shock to shift its position to accommodate the modified pressure field, but the shift in the shock position modifies the shape of the boundary layer separation. This process continues over and over and establishes a recursive interaction that produces self-sustained shock oscillations.

A model describing the mechanisms of self-sustained shock oscillations was presented by Lee (2001). The following equation expresses the total time it takes for a disturbance

originating from a shock to complete a full cycle:

$$T_p = \int_{x_s}^{c} \frac{1}{a_p} dx - \int_{c}^{x_s} \frac{1}{a_u} dx. \tag{1.15}$$

In this equation, the first term expresses the time it takes for a disturbance to propagate through the separated region from the base of a shock to the tail edge of the airfoil, and the second term expresses the time it takes for the disturbance to propagate back to the shock through the free stream. The velocity of a pressure wave in the boundary layer, a_p, can be approximated by measuring the pressure gradient across the surface of the airfoil and relating the phase angle with the coefficient of chord length, x/c. To calculate a_u, Lee used the approximation

$$a_u = (1 - M_{loc}) a_{loc}, \tag{1.16}$$

which was given by Tijdeman (1977). In Tijdeman's approximation, a_{loc} is the speed of sound, and M_{loc} is expressed as:

$$M_{loc} = R \left[M_{loc-S} - M_\infty \right] + M_\infty. \tag{1.17}$$

In this equation, M_{loc-S} is the Mach number at the surface of the airfoil, and M_∞ is the freestream Mach number. R is a relaxation factor set to 0.7. The oscillation frequency of the shock is then calculated by the inverse of T_p, $1/T_p$.

As Lee's model clearly illustrates, airfoils of different sizes will propagate disturbances at different rates. Therefore, it is useful to discuss shock oscillations in terms of reduced frequency, k. This is a nondimensionalized form of frequency, and it was demonstrated by Levy (1978) to be a valid method for dealing with scaling effects. Reduced frequency is calculated by:

$$k = \frac{2\pi f c}{U_\infty}, \tag{1.18}$$

where c is the chord length and U_∞ is the freestream velocity.

In the classical study performed by Tijdeman (1977), three different types of shock motion behavior were identified. The variation in the shock motion was dependent on how close or far away the freestream Mach number was to the critical Mach number. These three types of shock motion were dubbed Type A, B, and C (not to be confused with Type A and B boundary layer separation) and are illustrated in Fig. 1.10. When the freestream Mach number is close to the critical Mach number, certain phases of the tail flap oscillation cycle cause the flow on one side of the airfoil to retreat back to only being subsonic flow, and the shock vanishes on that surface. As the freestream Mach number rises further from the critical Mach number, the ability of the flap to induce subsonic flow diminishes, and the flap motion no longer causes the shock to periodically vanish.

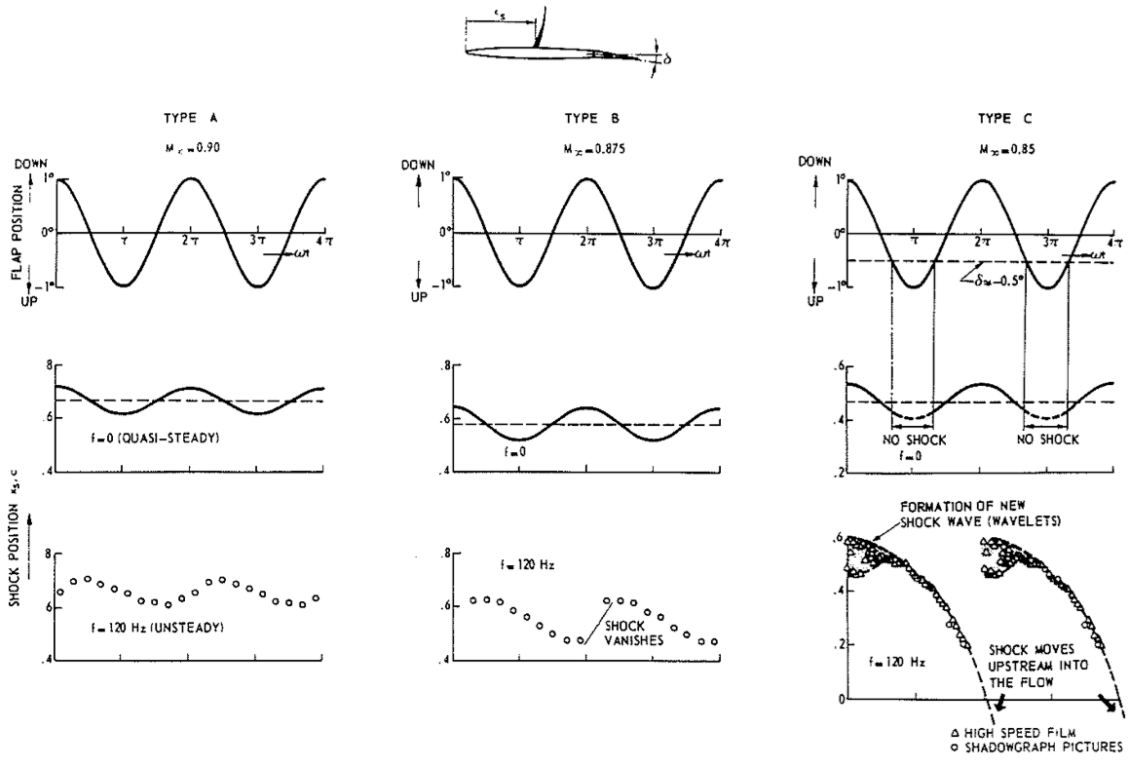

Figure 1.10. Tijdeman's Classifications of Shock Motion (Tijdeman, 1977)

Bruce & Babinsky (2010) studied the relationship between shock motion and downstream

pressure fluctuations using a parallel walled duct in order to eliminate unsteady effects caused by geometry. An elliptical blocking mechanism located downstream of the test section was set up to rotate at various frequencies in order to create periodic downstream pressure fluctuations. The frequency of the shock motion detected during each tunnel run was close to that of the downstream pressure fluctuations. Bruce & Babinsky also found that the shock velocity was virtually independent of the frequency of the pressure fluctuations, and thus the shock motion amplitude decreased as the fluctuation frequency increased.

Raveh & Dowell (2011) studied the effect of an oscillating airfoil on the shock motion. The shock oscillation frequencies were found, for certain combinations of airfoil motion frequencies and amplitudes, to synchronize with the airfoil's oscillation frequency. This suggests that there is a relationship between shock oscillation frequencies and the first torsion structural mode of an airfoil.

1.3.1 The Buffet Boundary

One of the primary goals of buffeting research is to glean a method for predicting when buffeting will occur. Pearcey, as cited by Lee (2001), developed one of the earliest methods for determining the onset of buffeting that was based on the growth of bubble separation. The basis of this method is that once the separation bubble reaches the tail edge and then bursts, it creates a steep pressure divergence that induces buffeting. The method requires pressure measurements of the trailing edge, which can be cumbersome to obtain, and when this method was used by DeAngelis & Monaghan (1977), it worked well for lower subsonic Mach numbers but not higher ones.

Erickson (1974) presented a method for predicting the onset of buffeting based on the structural response of an airfoil by measuring the bending stress on the airfoil. Lee & Tang (1988) used a similar method based on the divergence of the unsteady normal force on an airfoil. These methods both gave reasonable results and require minimal instrumentation.

Thomas, as cited by Lee (2001), developed a method similar to Pearcey's bubble separation bursting method. Instead of basing the criterion on when the separation bubble

reaches the tail edge, he set the mark at the position $x/c = 0.9$ on an airfoil. Lee (2001) discusses how this method has been used for conventional and supercritical airfoils and in experimental and computational studies, and has given satisfactory results in all cases.

All of these methods stem from two fundamental concepts; measuring either surface pressures on an airfoil or structural responses within an airfoil. Lee (2002) discusses how these two approaches are rooted in statistical theory and suggests that each one yields reasonable results but have various pros and cons in their implementation and insights. Crouch *et al.* (2009) proposed that buffeting onset is better thought of as a stability problem and illustrated how global stability analysis yields better results for predicting buffeting onset than previous empirical models do.

1.3.2 Methods for Controlling Buffeting

While many studies have focused on the pursuit of understanding the onset and behavior of buffeting, other studies have investigated methods of controlling buffeting. Chen (1985) studied the effect of placing a porous surface underneath a transonic shock and found that the porous surface increases lift and reduces drag due a reduction in the pressure jump across the transonic shock. The potential of this technique to control buffeting was later tested by Tulita *et al.* (1995) and Doerffer & Szulc (2006), and it was found to be effective at buffet alleviation. In an experiment similar to Chen (1985), Seifert & Pack (1999) used an active blowing system instead of a passive one to reduce shock strength and buffeting. The relationship between buffeting and the surface geometry under a shock was further investigated by Tulita *et al.* (2004) by placing a contoured bump underneath a transonic shock. This resulted in drag reduction and buffet alleviation effects similar to those of a porous surface.

Lee & Tang (1988) built off of the work performed by Tijdeman (1977) and showed that a trailing edge deflector could effectively stave off buffeting to a higher freestream Mach number than normal, and this result was later studied and confirmed by Despre *et al.* (2001).

Raghunathan *et al.* (1999) studied the reduction of buffeting by placing a splitter plate at the tail edge of an airfoil to divide the top and bottom sides of the wake. This approach is impractical by itself since it would interfere with lift, but it did alleviate buffeting. These studies illustrate the significance that controlling the communication between the top and bottom sides of an airfoil at its tail edge can have on controlling buffeting.

1.4 Present Study

The purpose of the present study is to contribute to the growing body of knowledge on buffeting by analyzing the effects that the angle of incidence of an airfoil has on transonic shock oscillations. Wind tunnel runs were conducted using a NACA 0018 model at varying angles of incidence, and high-speed schlieren images were taken to create a time series of shock positions for each angle. A unique computer algorithm, outlined in Section 3.2, was developed to analyze the frequency of shock motion by determining the dominant frequencies for an array of points in space. With the assumption that the shock motion is responsible for the dominant frequencies in that space, the location of the peaks in the frequency domain reveals the range of shock motion as well as the frequency at which the shock moved. From this information, a relationship is drawn between the angle of incidence and the shock oscillation frequency.

Chapter 2 describes the experimental setup, including the design and construction of the airfoil model, the calibration and settings used for the wind tunnel, and the data acquisition method. Chapter 3 describes the computer algorithm used to analyze the data. In addition, it describes various other algorithms that were developed, but whose results were less reliable. Chapter 4 presents the results obtained from that code and discusses conclusions drawn from them, and Chapter 5 suggests future work to build on the present study.

CHAPTER 2

THE EXPERIMENT: DESIGN, SETUP, & EXECUTION

The experimental data for this study was obtained using the 12-inch trisonic wind tunnel at the National Center for Physical Acoustics (NCPA). Section 2.1.1 discusses the design and implementation of the airfoil model. In order to use the NCPA's wind tunnel for the present study, the wind tunnel was configured for transonic operations. Section 2.2 discusses the configuration and the calibration of the wind tunnel for running at transonic conditions. A Photron FASTCAM high-speed camera in combination with a schlieren system was used as the primary data acquisition method. Section 2.3 discusses the data acquisition methods that were used in the present study

2.1 Airfoil Model Design

2.1.1 Airfoil Profile

The airfoil profile used in the present study was a NACA 0018, and this airfoil is shown in Fig. 2.1 compared to the widely studied NACA 0012. The NACA 0018 is a symmetrical airfoil in the NACA four-digit series, and its profile is calculated using the formula

$$y = \frac{t}{0.20}(0.2969\sqrt{x} - 0.1260x - 0.35160x^2 + 0.28430x^3 - 0.10150x^4), \qquad (2.1)$$

where t is the maximum percent thickness of the airfoil. In the NACA four-digit series, the first two digits in the name of the airfoil denote the airfoil's camber, and the last two digits denote the airfoil's maximum percent thickness (Jacobs *et al.*, 1935).

The primary limiting factor governing the size of the model was that it needed to be small enough to not create a tunnel blockage of greater than 4%. Setting the chord length to

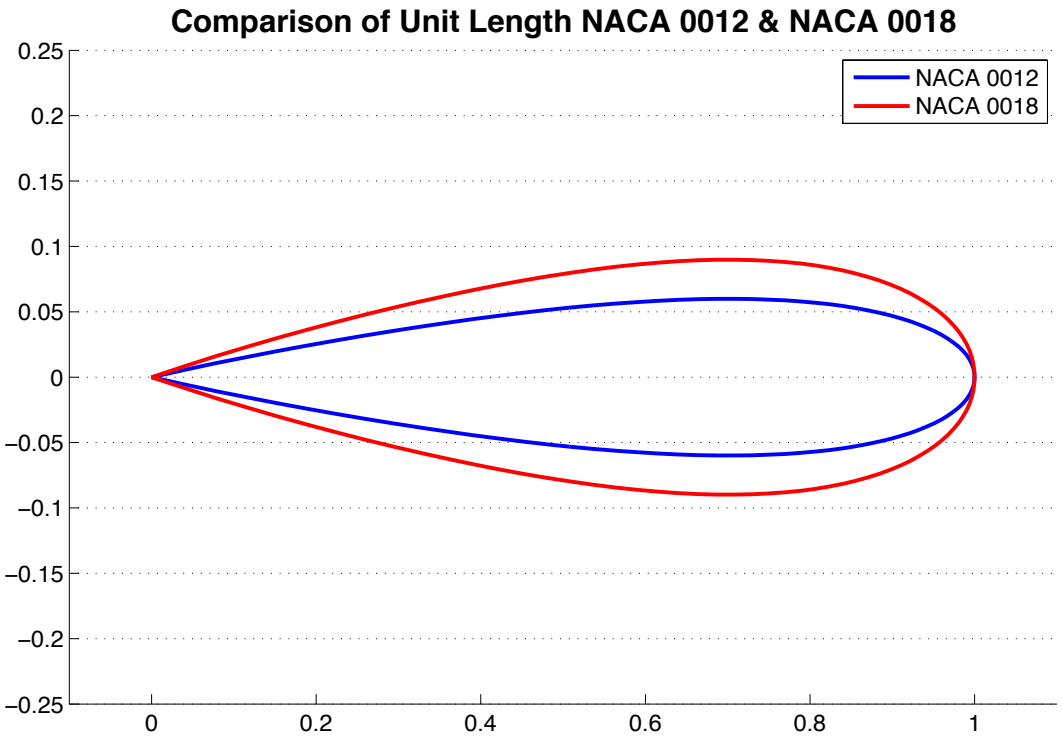

Figure 2.1. Shape Comparison of NACA 0012 and NACA 0018 Profiles

3 inches gave a maximum thickness of 0.54 inches, and then setting the width of the model to 6 inches yielded a maximum total cross-sectional area normal to the flow of 5.06 inches^2 or 3.51% tunnel blockage. Furthermore, this model size produces enough space for pressure sensors to be installed for future studies.

2.1.2 Mounting the Airfoil Model

The NCPA's wind tunnel has two options for mounting a model inside it. One option is to mount the model directly to the floor plate of the tunnel's test section, and the other is to use the wind tunnel's model support system. Both would provide ample support and would make it relatively easy to route instrumentation to the model, but the latter was used for the present study because it enabled the adjustment of the model's angle. The model support system, illustrated in Fig. 2.2, is located downstream of the test section and is capable of independently adjusting a model's vertical position by ± 3 inches and pitch

angle by ± 20°, which allowed for sufficient maneuverability for the desired testing range of 0° to 6° incidence.

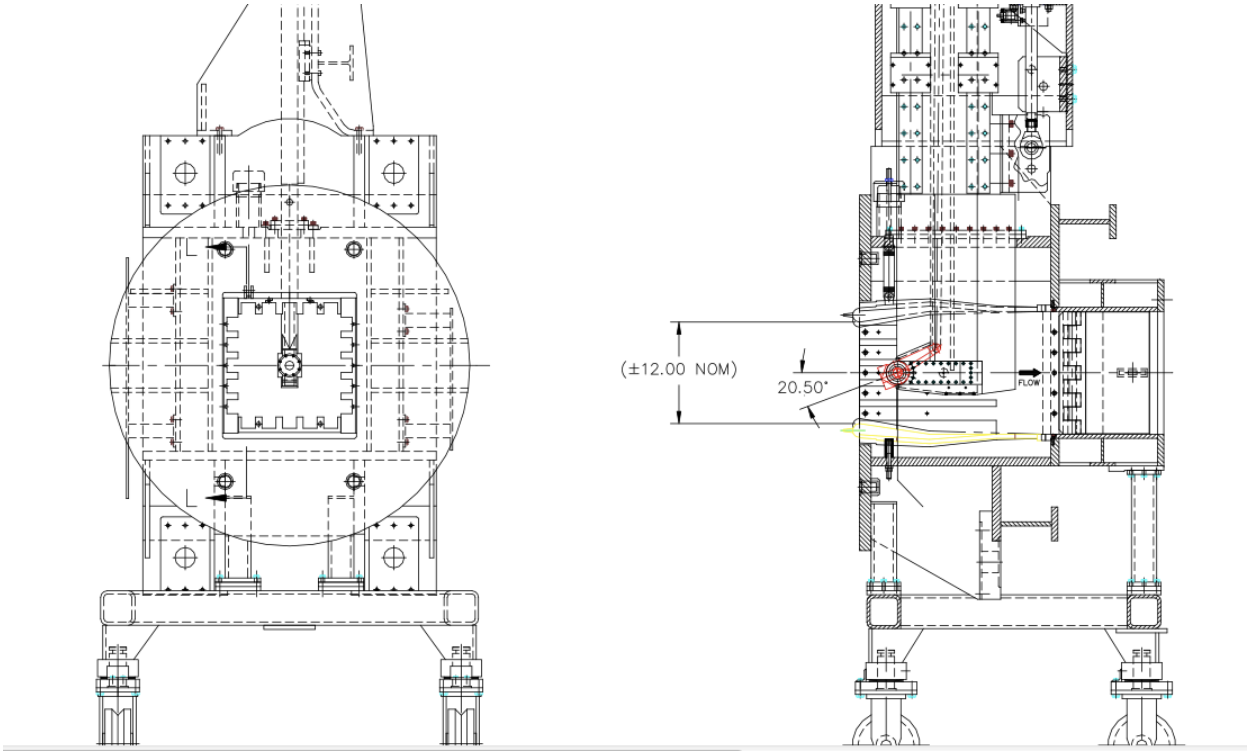

Figure 2.2. Diagram of Model Support System in NCPA's Wind Tunnel

2.1.3 Model Positioning

Extension Arm

The model support system required an extension arm to allow the model to reach into the test section, and there were three chief concerns for designing this extension arm. First, it had to be 10 inches long in order to reach the test section. Second, it needed to have a hollow inner diameter of 0.5 inches to allow instrumentation to be routed to the model. Third, the extension arm required an outer diameter of 1.25 inches so that it would be large enough to house female threading for attaching to the model support adapter, which is shown in Fig. 2.3.

A stock stainless steel hollow rod was obtained from a supply company, and after minimal machining it was modified to meet the required specifications for the extension arm. The

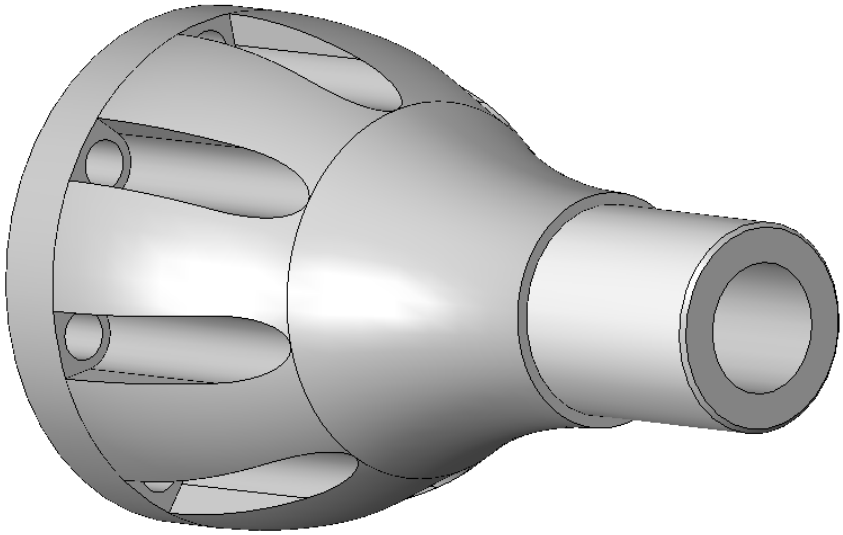

Figure 2.3. CAD of the Model Support Adapter

upstream end of the extension arm was formed into a horseshoe shape, shown in figure 2.4, which was designed to mate with a bullet-nosed cap (discussed below). The horseshoe shape provided support against torsional loads that could act on the model during startups. Three screw holes were drilled into the extension rod around the horseshoe protrusion so that the bullet-nosed cap could be secured to it.

Bullet-Nosed Cap

The bullet-nosed cap, shown in Fig. 2.5, was designed using the equation for a bullet-nose curve:

$$x^2y^2 = a^2x^2 - b^2y^2, \tag{2.2}$$

where a = 0.716 and b = 1.12. These values were concluded empirically such that the rear diameter would match the extension arm's outer diameter. The bullet-nose shape was chosen to help mitigate the formation of vortex shedding on the extension arm.

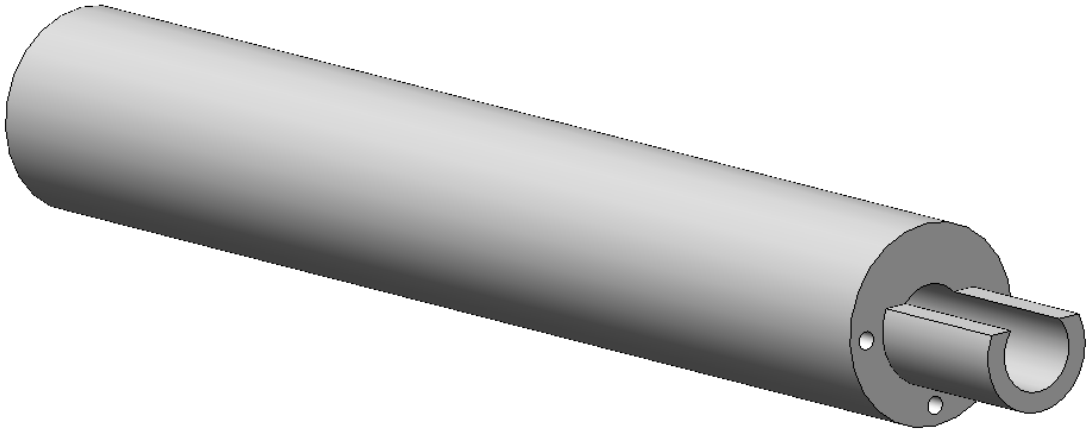

Figure 2.4. CAD of the Extension Arm

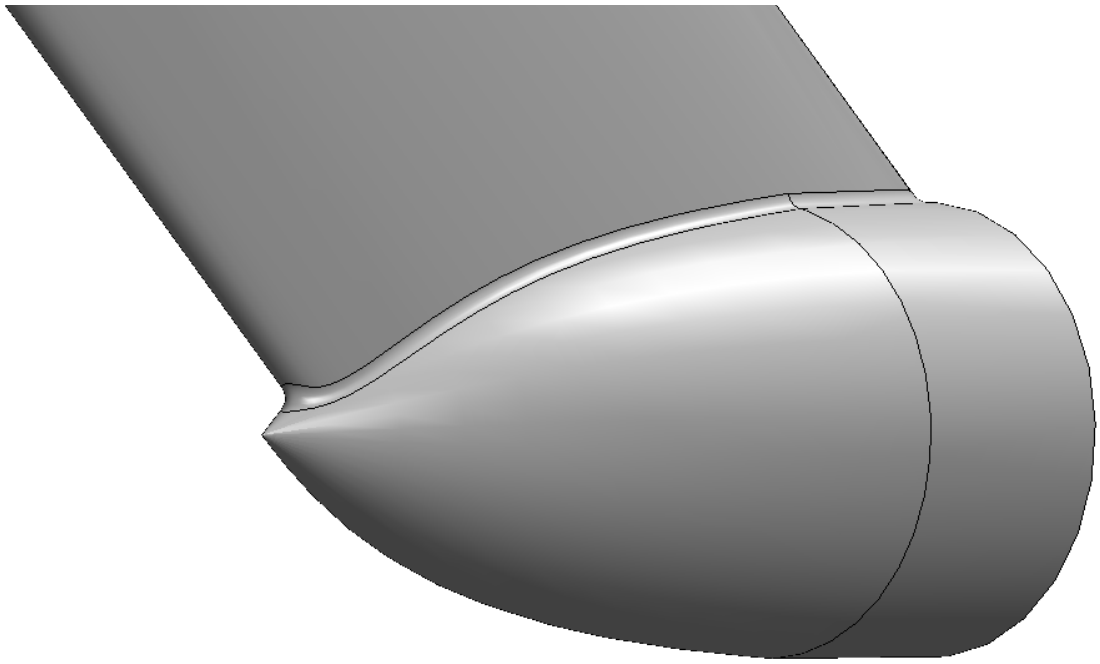

Figure 2.5. CAD of the Bullet-Nosed Cap and Strut.

Strut

A strut was used to attach the airfoil model to the bullet-nosed cap. The strut extended at a 45° angle from the extension arm to help prevent any flow structures originating from the extension arm from interacting with the airfoil model. The shape of the strut was designed based on the NACA/Langley Symmetrical Supercritical airfoil profile, which is shown in Fig. 2.6. Since this is a symmetrical, supercritical airfoil, it helps to prevent transonic shocks from forming on the strut and produces no lift forces at 0° incidence. The chord length of the strut was 3 inches, corresponding with the model chord length. This resulted in the maximum thickness of the strut being 0.33 inches and yielded a cross-sectional area of approximately 1 inch^2.

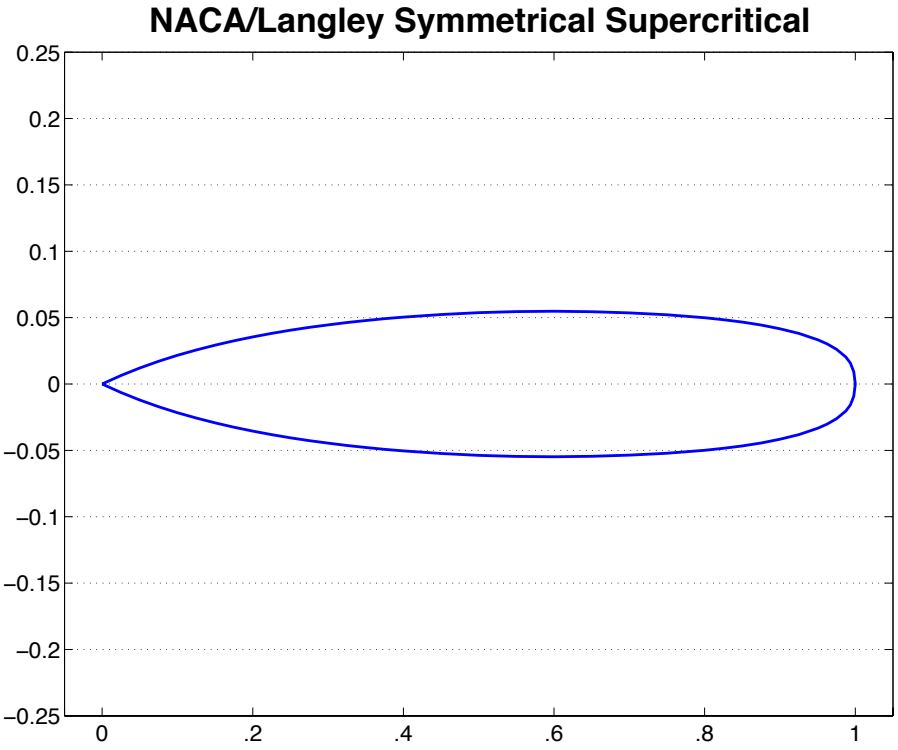

Figure 2.6. NACA/Langley Symmetrical Supercritical Airfoil Profile

2.1.4 Material

The airfoil model was constructed by stereolithography (3D printing) using the material Accura 60. This allowed the bullet-nosed cap, strut, and airfoil to all be fashioned as one piece, shown mounted on the model support in Fig. 2.7, and this approach comprised two primary merits. First, it alleviated the need to design connection joints for the smaller, more awkwardly shaped pieces of the model. Second, the tensile strength of Accura 60 is rated between 8,410 to 9,860 psi (3D-Systems, 2006). This is more than adequate for the present study, which can be illustrated by examining the weakest point of the airfoil model, the connection between the strut and airfoil. This joint has a cross-sectional area of 1 inch^2. The lifting force of an airfoil is calculated by

$$L = C_L A \; q, \tag{2.3}$$

where C_L is, in this case, a function of the angle of attack. The largest angle used in the present study was 6°, which produces a lift coefficient of 0.66 (Sheldahl & Klimas, 1981). Therefore, the greatest lift force expected to be produced by the airfoil was 71.28 lb., which is far below the limitation of the Accura 60 plastic.

2.2 Transonic Tunnel Configuration

The NCPA's wind tunnel is primarily used for supersonic testing and had not been operated under transonic conditions prior to the execution of the present study. Therefore, the first order of business was to reconfigure the wind tunnel and assemble it with the transonic cart. The fully assembled wind tunnel is shown in Fig. 2.8.

2.2.1 Transonic Cart

There are two primary components to the transonic cart: the transonic nozzle and the transonic test section. Unlike a supersonic nozzle, which converges and diverges before the flow enters the test section, a transonic nozzle only converges as the flow enters the test

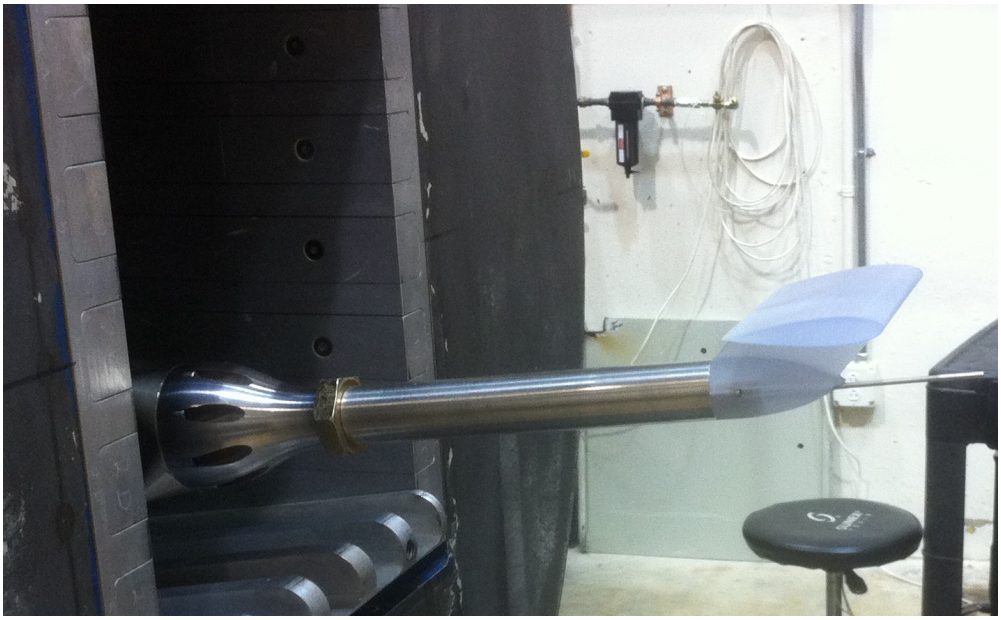

Figure 2.7. Airfoil Model Assembled on the Model Support System

section. The test section, which is shown disassembled in figure 2.9, then acts as the throat of the nozzle.

The other key feature of the transonic test section is the presence of wall perforations, shown in Fig. 2.10. The perforations allow suction to be applied to the test section to reduce wall reflections of shocks originating from the model, which would interfere with the flow field in the test section. A detailed overview of the effects of perforated wind tunnel walls can be reviewed in a variety of studies (Chew, 1953; Capone, 1995; Ewald *et al.*, 1998; Mokry *et al.*, 2000; Krynytzky, 2001; Lockheed-Martin, 2002; Thiery & Coustols, 2006).

2.2.2 Transonic Flow Velocity Calibration

The present study was the first use of the NCPA's transonic cart other than when it was tested during its construction. Therefore, before installing the airfoil model into the wind tunnel, calibrations were performed using a pitot probe mounted on the model support system which is shown in Fig. 2.11. The tunnel flow velocity is controlled by a combination of regulating the pressure from the inlet tank, adjusting choke flaps located downstream of the test section, and applying plenum suction to the test section.

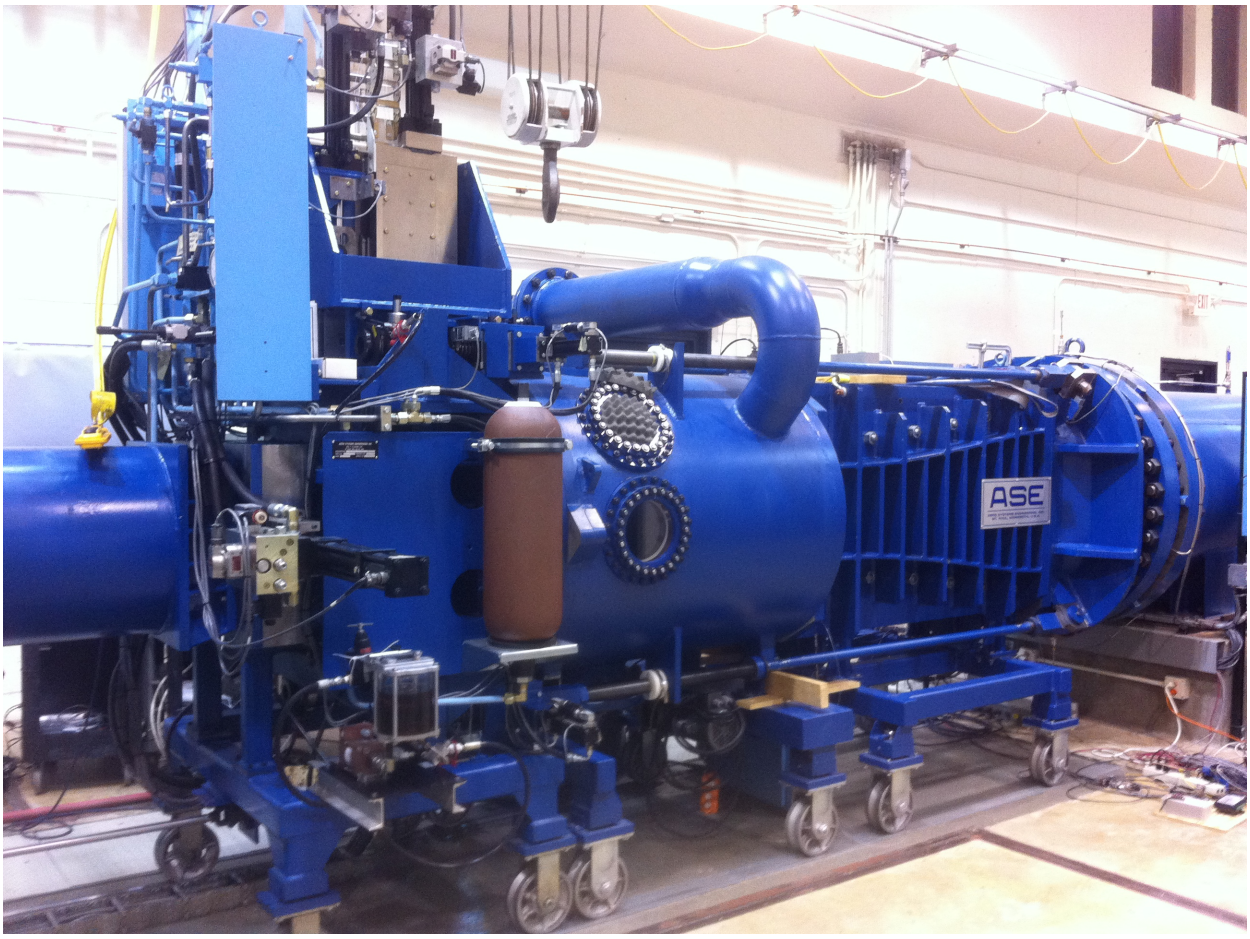

Figure 2.8. The NCPA's Fully Assembled Transonic Tunnel

The target Mach number for the present study was not known and had to be determined empirically because the buffet boundary for a NACA 0018 had not been previously established in any of the literature reviewed by the current author. In order to address this, the critical Mach number for a NACA 0018 was calculated using the procedure outlined in Section 1.1.4 and found to be 0.66, and this velocity was used as a starting point for determining the buffet boundary. Once the flow control settings were established for running at Mach 0.66, the pitot probe was then situated protruding from the bullet-nosed cap, shown in Fig. 2.12, in order to monitor the velocity near the airfoil model. The model was then installed into the wind tunnel at 0° incidence, and tunnel runs were conducted where the flow velocity was incrementally increased over a series of runs while schlieren imaging was

Figure 2.9. Installation of Windowed Walls into the Transonic Test Section

used to monitor shock formation and behavior on the model. Minor shocks were initially observed, and a classic transonic shock pattern developed once the freestream neared Mach 0.7. Type A shock oscillation began to occur as the flow velocity approached Mach 0.73 and a Reynolds number of $1.5 * 10^6$, so this was set as the freestream Mach number for the duration of the experiment.

Figure 2.10. Slotted Walls Inside the Transonic Test Section

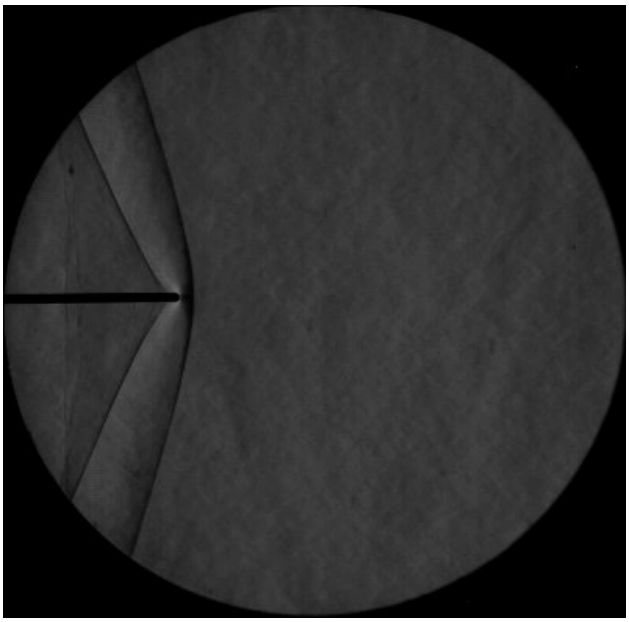

Figure 2.11. Pitot Probe Installed in Wind Tunnel Running at Mach 1

2.3 Schlieren Data Acquisition

Schlieren was used as the primary data acquisition method for the present study, and a comparison of a conventional photo and a schlieren photo is shown in Fig. 2.13. The

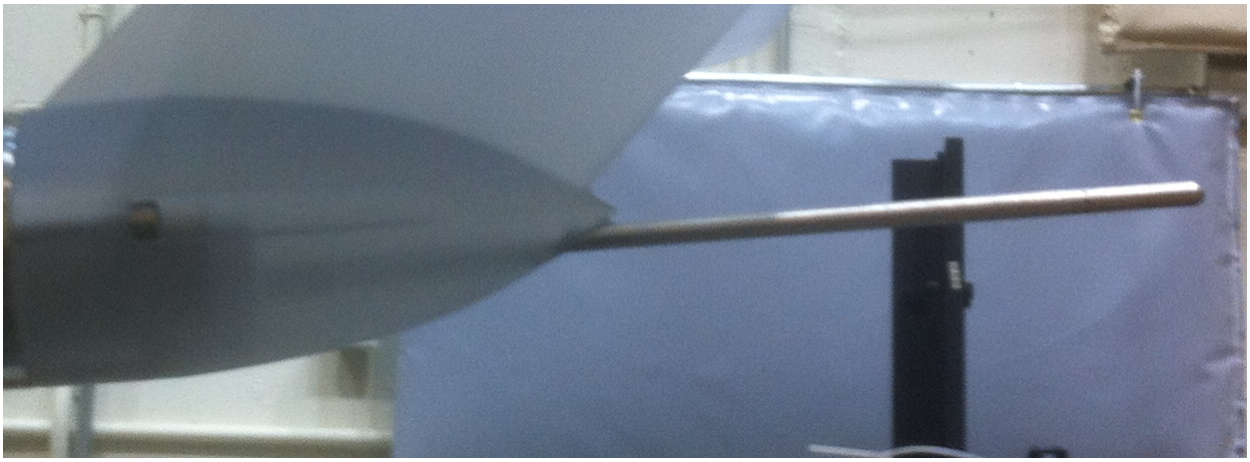

Figure 2.12. Pitot Probe Installed in the Bullet-Nosed Cap

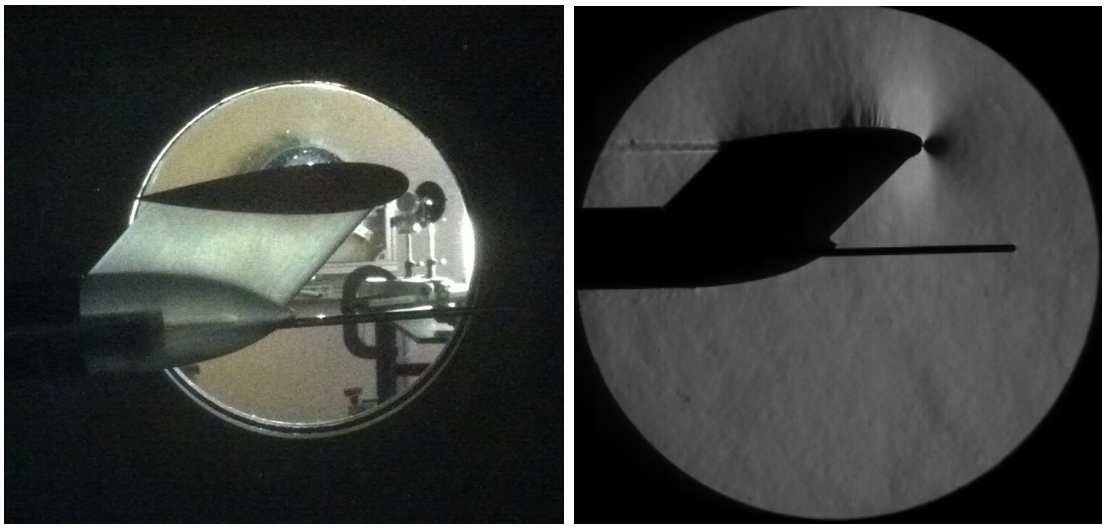

Figure 2.13. Comparison of Convetional Photo & Schlieren Photo of Airfoil in Tunnel

technique is theoretically based on the Gladstone-Dale equation,

$$n - 1 = k\ \rho, \tag{2.4}$$

which defines a relationship between the density of a gas and the index of refraction of light passing through the gas, and is a measure of the first derivative of the index of refraction, $\partial n/\partial x$. This phenomenon is normally masked due to the scattering of light, but when light is columnated, the effect can be readily observed. The method is utilized by passing a column

of uniformly intense light through a flow field with varying local densities and then focusing the light onto a surface that is partially blocked by a knife edge to enhance the contrast. The resulting image then clearly depicts the gradients in the flow field via the intensity gradient in the image. A thorough review of schlieren theory and applications is covered by Settles (2001).

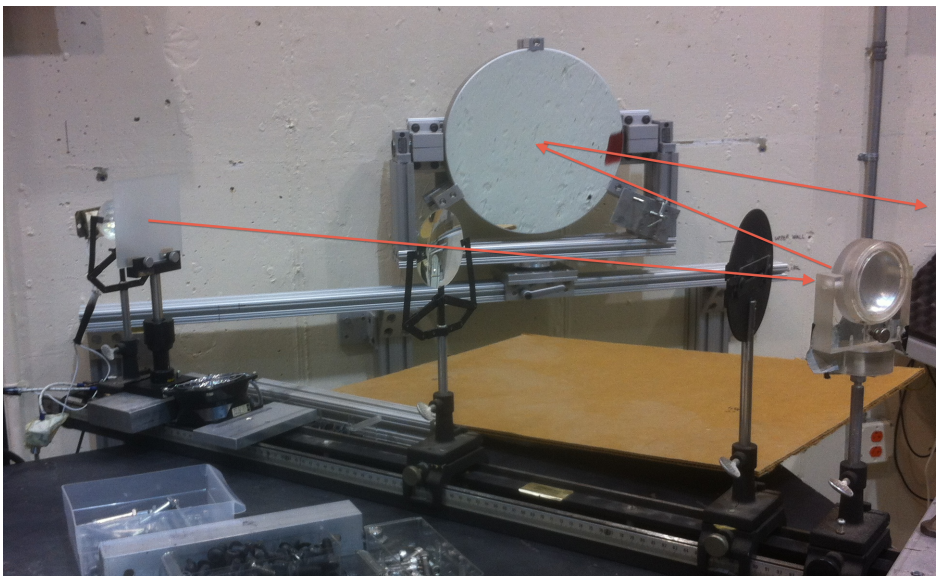

Figure 2.14. Path of Columnated Light Projected Through the Test Section

The NCPA's schlieren system is a Z-setup, and the lens configuration that columnates the light and sends it into the wind tunnel test section is shown in Fig. 2.14. The arrangement consists of a light source that shines through a slit onto a turning mirror that projects the light onto a 15-inch parabolic mirror. The light that reflects off of the 15-inch mirror is a parallel column of light that passes through the test section of the wind tunnel and onto a second 15-inch parabolic mirror which is shown in Fig. 2.15. This mirror refocuses the light onto the lens of a high-speed CCD camera that is partially blocked by a razor blade to produce the schlieren effect.

The high-speed camera used in the present study was a Photron FASTCAM-Ultima APX. It was set to record 4,000 images per second for 3.072 seconds. This configuration yields 12,288 images per tunnel run, with each pixel representing a distance of 0.02 inches.

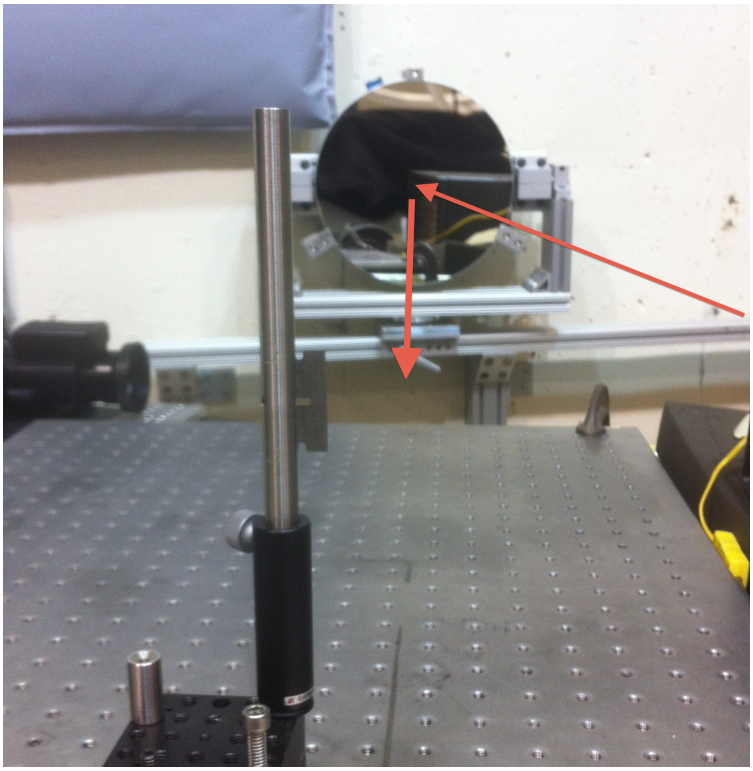

Figure 2.15. Path of Columnated Light Focused onto the Camera

CHAPTER 3

ANALYSIS METHODOLOGY

The schlieren data acquired from the present study produced a total of 86,016 images. In order to analyze the frequency of the shock motion from this multitude of data, an image processing method had to be developed to identify and locate the position of the transonic shock in each image. Seven different computer codes were written in the attempt to achieve sufficient, reliable results. The first six codes are discussed in Section 3.1, and the code that was ultimately used for the present study is discussed in Section 3.2.

3.1 Initial Analysis Approaches

The six methods that were initially developed all relied on the user isolating a two-dimensional structure that represented the shock, and the code then located and marked that structure in each time-slice image. Although these methods often produced veracious results, they were inherently unreliable due to the variability of user input and the existence of other flow structures such as turbulence that would sometimes be mistaken for the shock. Each method yields a series of values that represents the shock position for each image, and a fast Fourier transform (FFT) is then performed on the time series of these values to identify the frequency of motion. The following is a brief summary of the six algorithms that were not used.

1. The user-selected region was averaged into a 1-D profile of the intensity gradient. The same procedure was then performed across the top of the airfoil to produce a profile for each image, which was then correlated with the user selection profile. The position of the maximum correlation was then marked as the location of the shock for each image.

2. A 2-D correlation was performed between the user-selected region and the region spanning the top of the airfoil for each image. The position of the maximum correlation was then marked as the location of the shock for that image.

3. The region spanning the top of the airfoil, with the height of the user's selection, was averaged into a 1-D profile of the intensity gradient. The position of the maximum value along the resulting profile was marked as the position of the shock for each image.

4. The region spanning the top of the airfoil was averaged into a 1-D profile of the intensity gradient and the derivative of the profile was then taken. The position of the maximum value of the derivative was then marked as the location of the shock for each image.

5. The user-selected region and the region spanning the top of the airfoil were averaged into 1-D profiles of the intensity gradient, and the first derivative was performed on each profile. A correlation was then performed between each derivative and the derivative of the user selection profile. The position of the maximum value of the correlation was marked as the position of the shock for each image.

6. The pixel intensities of the user-selected region were averaged into a single value for each image.

3.2 Spatial Power Spectral Density Distribution Algorithm

The spatial power spectral density (PSD) distribution method was ultimately used because it was not sensitive to the size of the region selected by the user, and was therefore much more reliable than the other methods. The user must only select an array of pixels that is one pixel high and parallel to the direction of shock motion, that is above the turbulent boundary layer separation, and that spans the full range of the shock motion. The shock motion's general range can be discerned easily by viewing the time series of images.

Because these are schlieren images, intensity shifts in the pixels represent density fluctuations in the flow field, and therefore the PSD of a pixel is directly indicative of the temperature and pressure fluctuations in each pixel's location. In the present study, the pressure fluctuations relating to the shock oscillation frequency are assumed to be responsible for the dominant frequency in the PSD of any pixel that is within the range of shock motion. For any pixel that is outside of that range, the dominant frequency is caused by random flow structures, and the PSD for those pixels will be much weaker than the PSD of the pixels in the shock motion range. Therefore, by calculating the PSD of each pixel and lining them up spatially, the code creates an image that clearly depicts not only the dominant frequency at which the shock oscillated, but also the precise range over which it did so.

The spatial PSD algorithm is as follows:

- Rotate all of the images so that the airfoil appears horizontal.
- Remove pixel intensity shifts due to background light.
- Prompt the user to select the array to be analyzed.
- Prompt the user to group consecutive images into appropriately sized time blocks. (For this experiment, three blocks were used, each containing 4,096 images, giving a frequency resolution of 0.97 Hz.)
- Perform an FFT on each block of images, and determine the PSD for each pixel according to the PSD calculation outlined by Bendat & Piersol (2000).
- Average together each pixel's output from the different time blocks. (This process helps to accentuate steady frequencies and mitigate frequency anomalies.)
- Plot the data as frequency vs. spatial domain, with the frequency amplitudes in the z-axis.

The results generated by this method for the present study are presented in Section 4.1, and the complete code is included in Appendix B.

CHAPTER 4

RESULTS, DISSCUSSION, & CONCLUSION

4.1 Results & Discussion

Figures 4.1 through 4.7 present the results for the seven angles tested in the present study. There are two images included for each angle. The first image displays the output obtained from the spatial PSD distribution algorithm. The precise values are labelled for the peak frequency location. The second image displays the average grayscale value of the time series for that angle. This indicates the mean shock position, represented by the boundary between the dark region and the light region downstream of it. The user-selected pixel array is highlighted for reference by the horizontal line.

Fig. 4.8 is a plot of the maximum frequencies obtained for each angle. A trendline was plotted that indicates an increase of 0.0205 reduced frequency per degree, or 10.8 Hz per degree for the airfoil used in the present study. The amplitude of shock motion was found to increase by 0.0067 chord lengths per degree, or 0.0201 inches per degree for this airfoil. Fig. 4.9 shows the relationship between angle of incidence and amplitude of shock motion. It was also found that the size of the boundary layer at the tail edge of the airfoil increased by 0.0288 chord lengths per degree, or 0.0864 inches per degree. Fig. 4.10 shows the relationship between angle of incidence and wake height.

In the time series of images from the present study, the upstream conditions appear steady, but the downstream conditions are very active. This is in agreement with other studies on shock oscillation and buffeting (Raghunathan *et al.*, 1999; Dussauge & Piponniau, 2008; Crouch *et al.*, 2009; Benard *et al.*, 2010; Raveh & Dowell, 2011; Hartmann *et al.*, 2012), and lends credence to the theory of buffeting proposed by Lee (2001). It can also be seen

that the boundary layer separation originated at the base of the shock, and is therefore Type A.

The overall range of measured frequencies was 279.3 to 354.5 Hz, which calculates to a reduced frequency range of 0.53 to 0.68. There are no previous studies on shock oscillations that used the NACA 0018 airfoil. However, McDevitt & Okuno (1985) studied the NACA 0012, at Mach numbers ranging from 0.72 to 0.8 at 4° and 6° incidence, and found reduced frequencies ranging from 0.38 to 0.55. The higher frequency range found in the present study is in accordance with a study by Humphreys (1951), which found that a reduction in airfoil thickness is accompanied by a reduction in buffeting.

The present study found a positive correlation between the frequency and amplitude of shock oscillations. Bruce & Babinsky (2010) found an inverse relationship between them, but these two studies are not analogous. In the study by Bruce & Babinsky, only fixed pressure pulsations were present because geometrical effects were controlled. This eliminated any pressure shifts due to boundary layer separation and downstream pressure recovery. In the present study, however, the geometrical effects were significant, causing large pressure pulsations as the kutta condition attempted to remain satisfied. These pulsations are induced by the magnitude of the unsteady pressure differentials that fluctuate across the wake, and their intensity is a result of the contour of the airfoil and the presence of Type A separation. This is the cause of the increase in shock motion amplitude.

4.2 Conclusion

The present study showed that a NACA 0018 ranging from 0° to 6° incidence experiences shock oscillations with reduced frequencies ranging from 0.53 to 0.68. As the angle increased, so did the frequency of shock oscillations, the amplitude of shock oscillations, and the size of the boundary layer at the tail edge. The frequency of shock oscillations increases by approximately 0.0205 reduced frequency per degree. The shock motion amplitude increases by approximately 0.0067 chord lengths per degree, and the size of the boundary layer at the

tail edge increases by approximately 0.0288 chord lengths per degree.

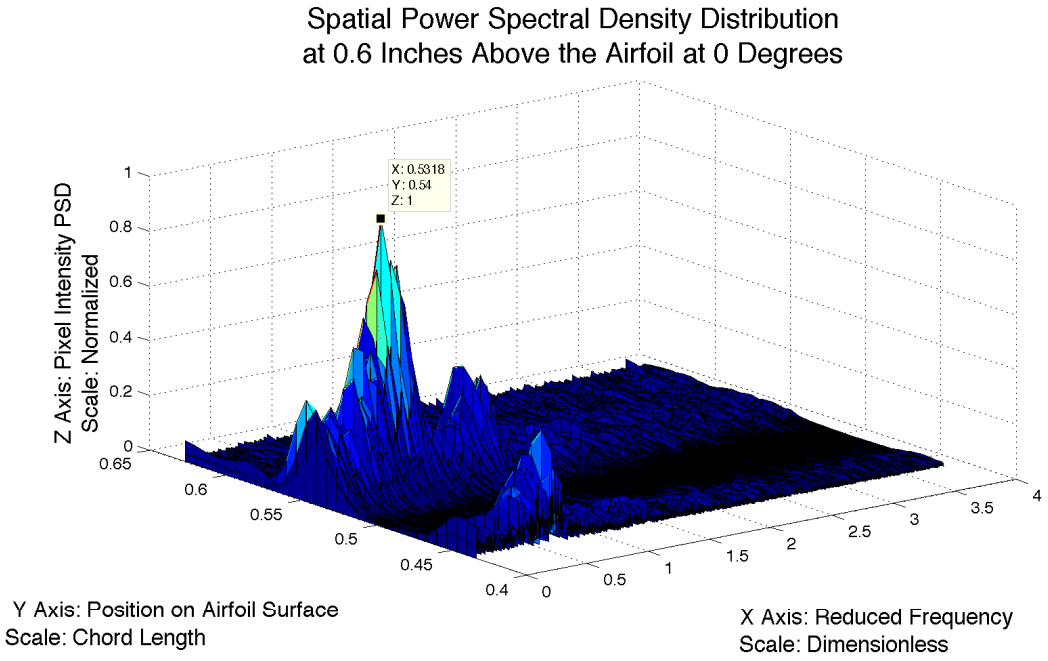

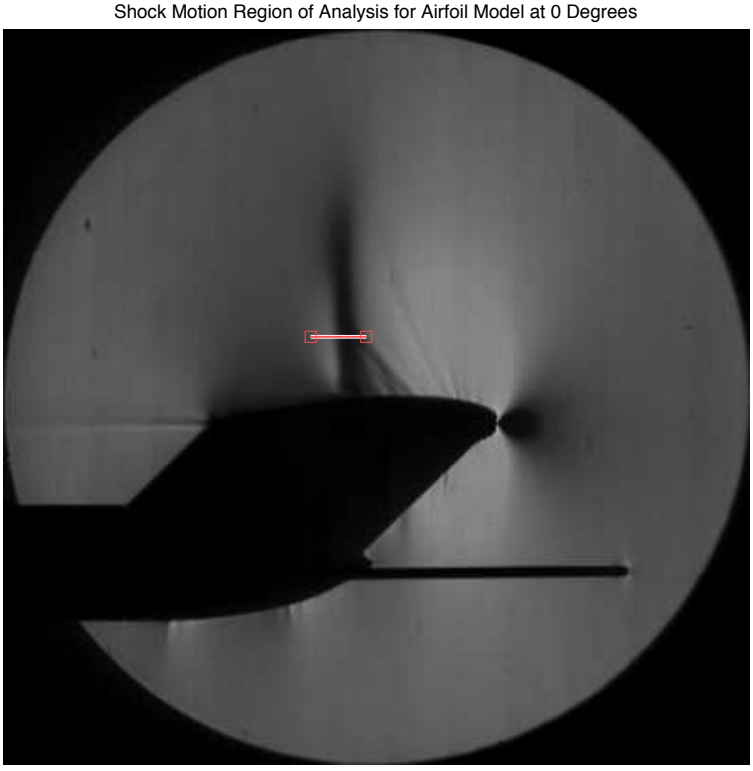

Figure 4.1. Spatial PSD Output (top) and Region of Interest (bottom) for 0° Incidence

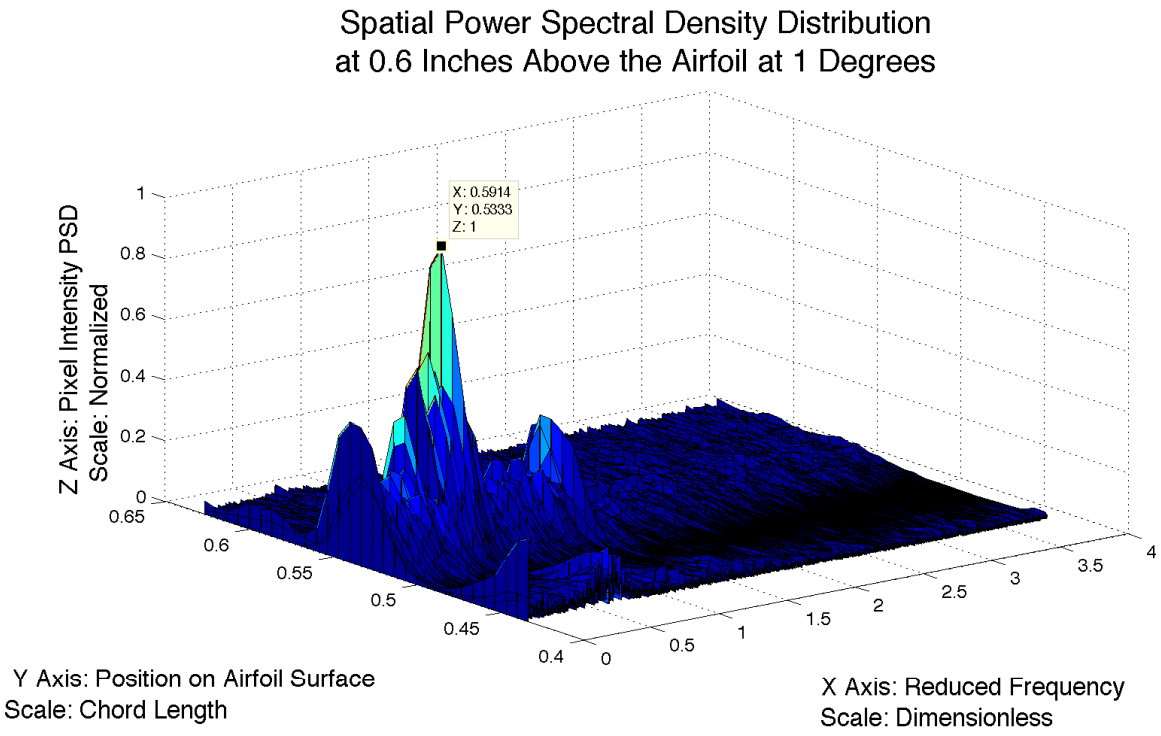

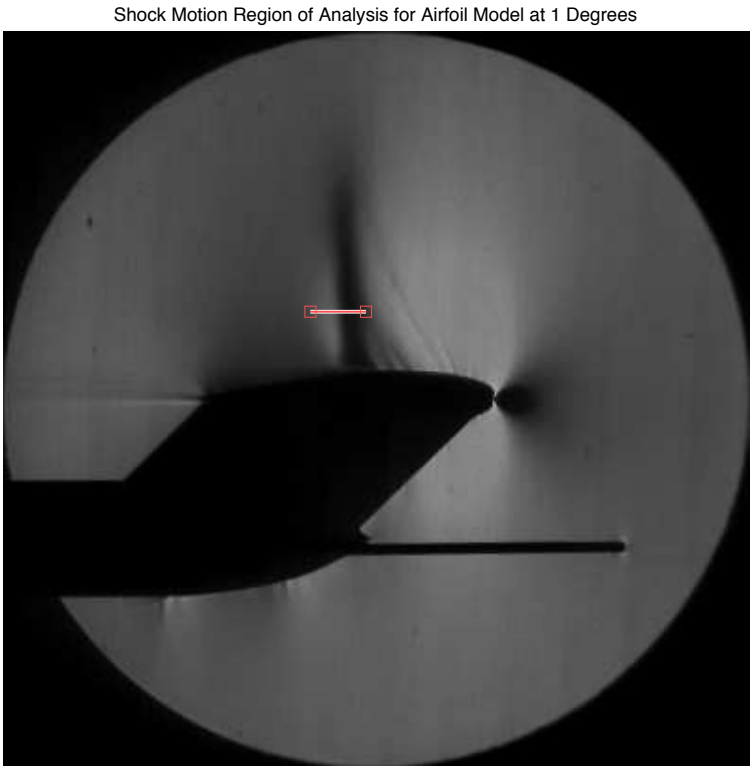

Figure 4.2. Spatial PSD Output (top) and Region of Interest (bottom) for 1° Incidence

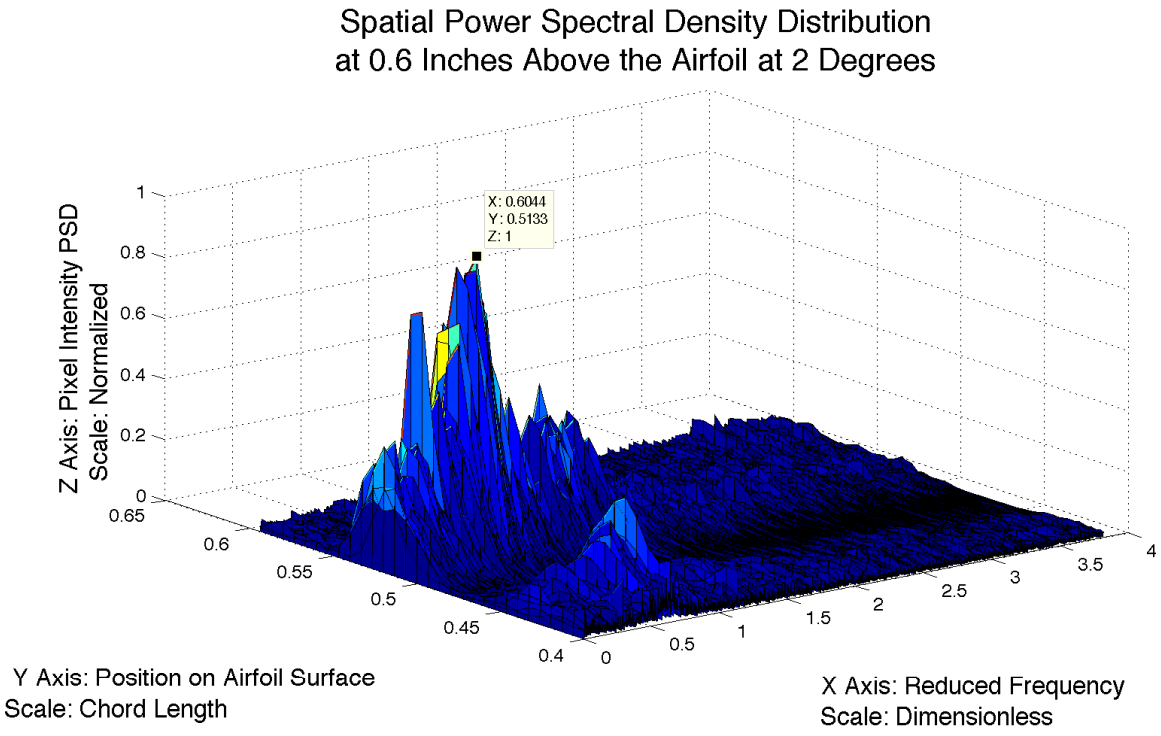

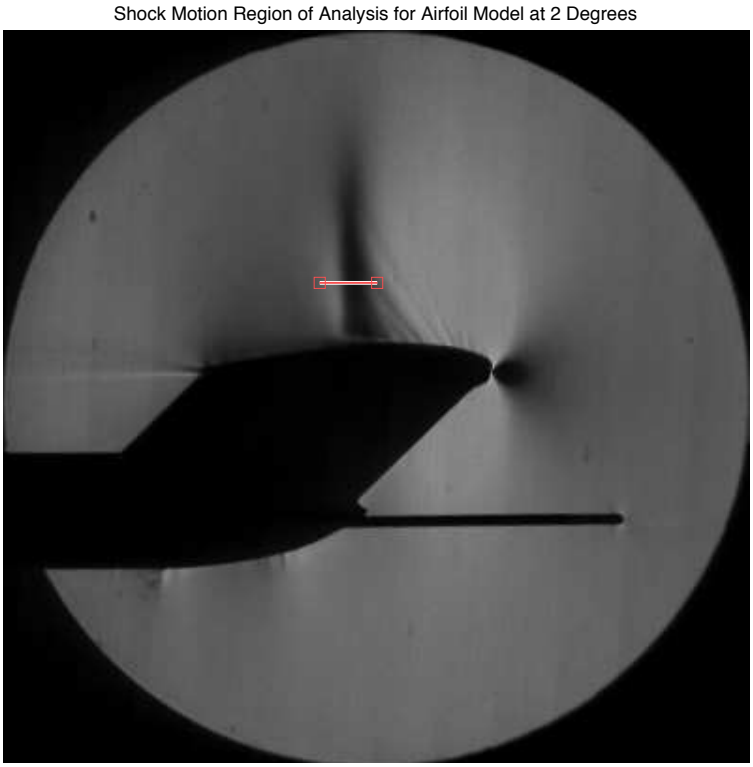

Figure 4.3. Spatial PSD Output (top) and Region of Interest (bottom) for 2° Incidence

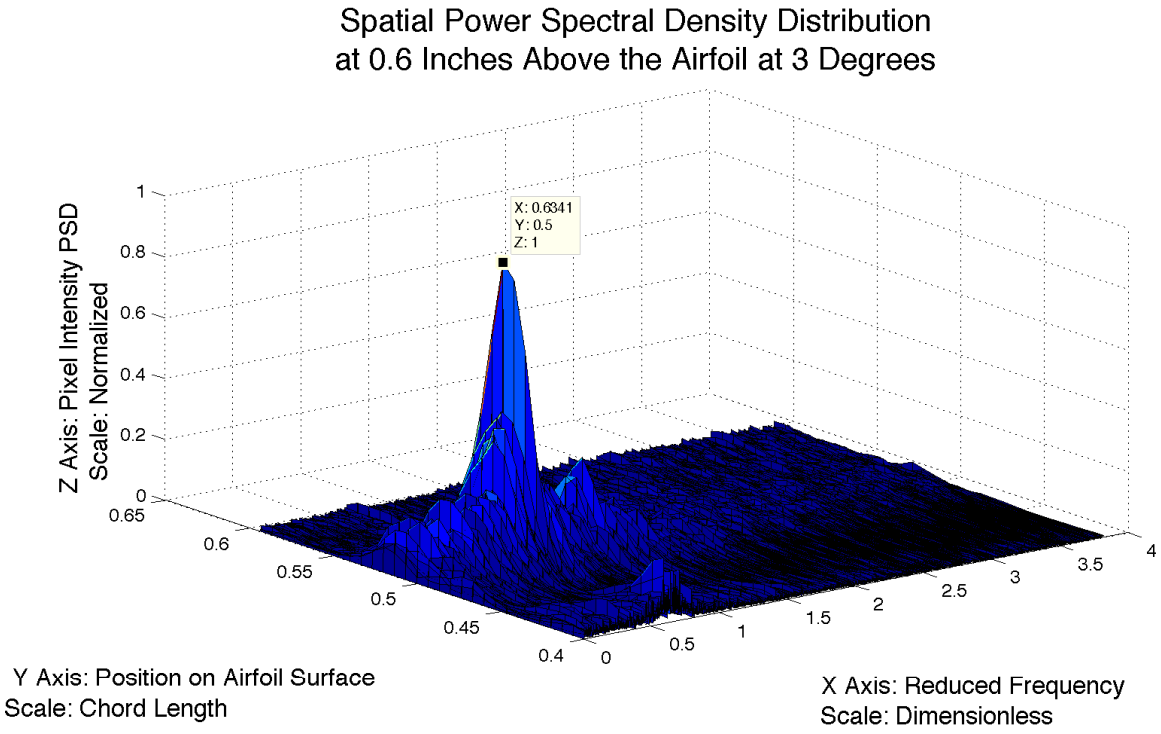

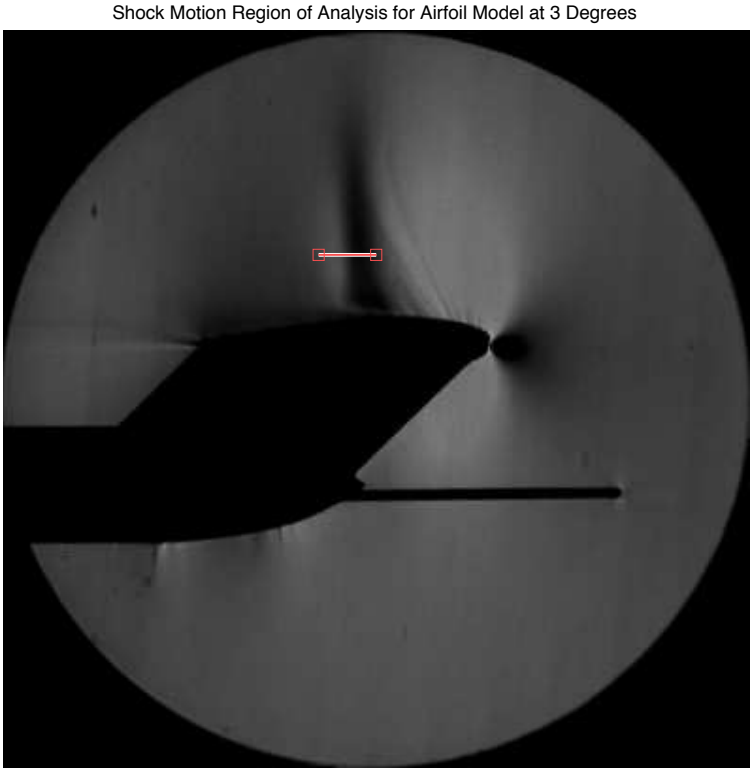

Figure 4.4. Spatial PSD Output (top) and Region of Interest (bottom) for 3° Incidence

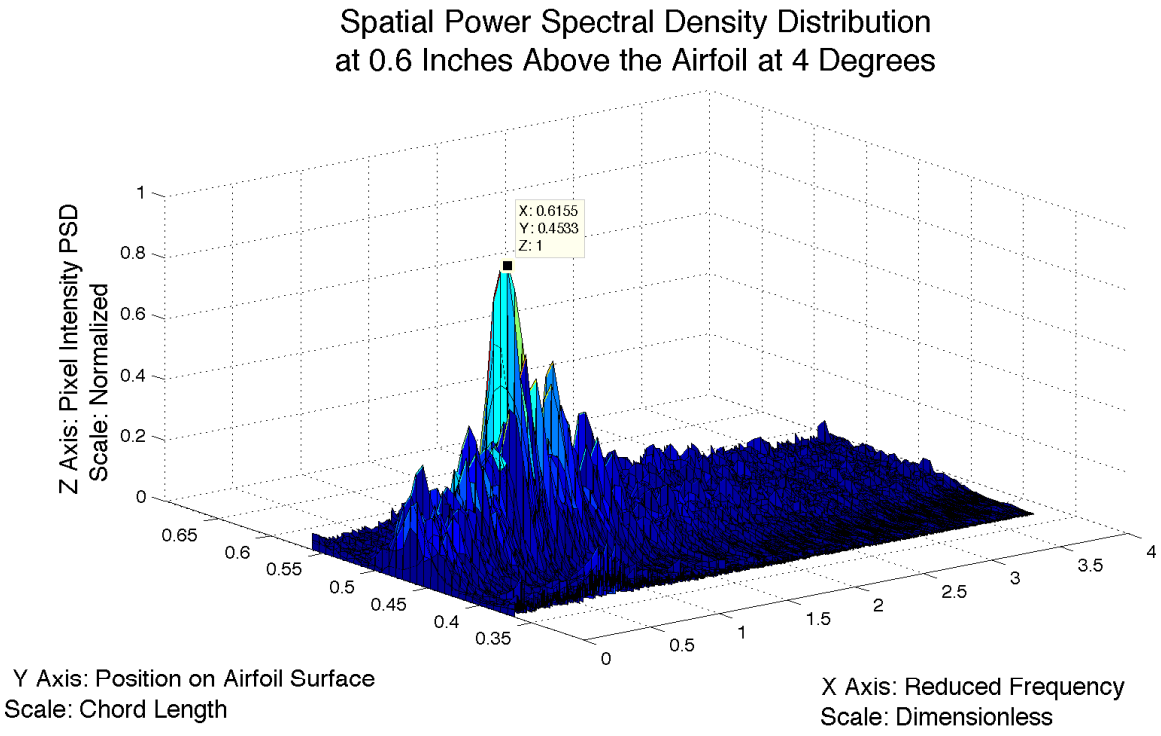

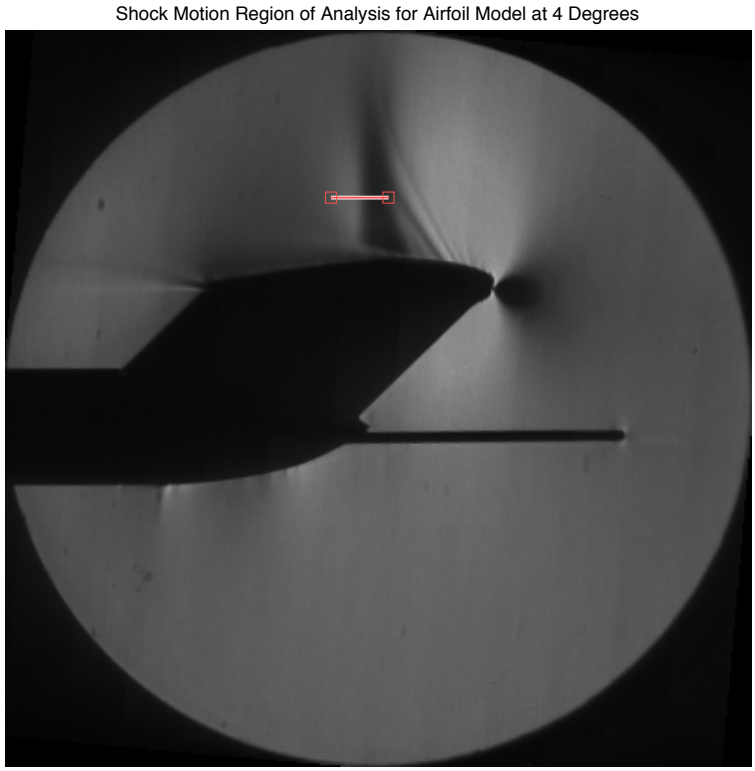

Figure 4.5. Spatial PSD Output (top) and Region of Interest (bottom) for 4° Incidence

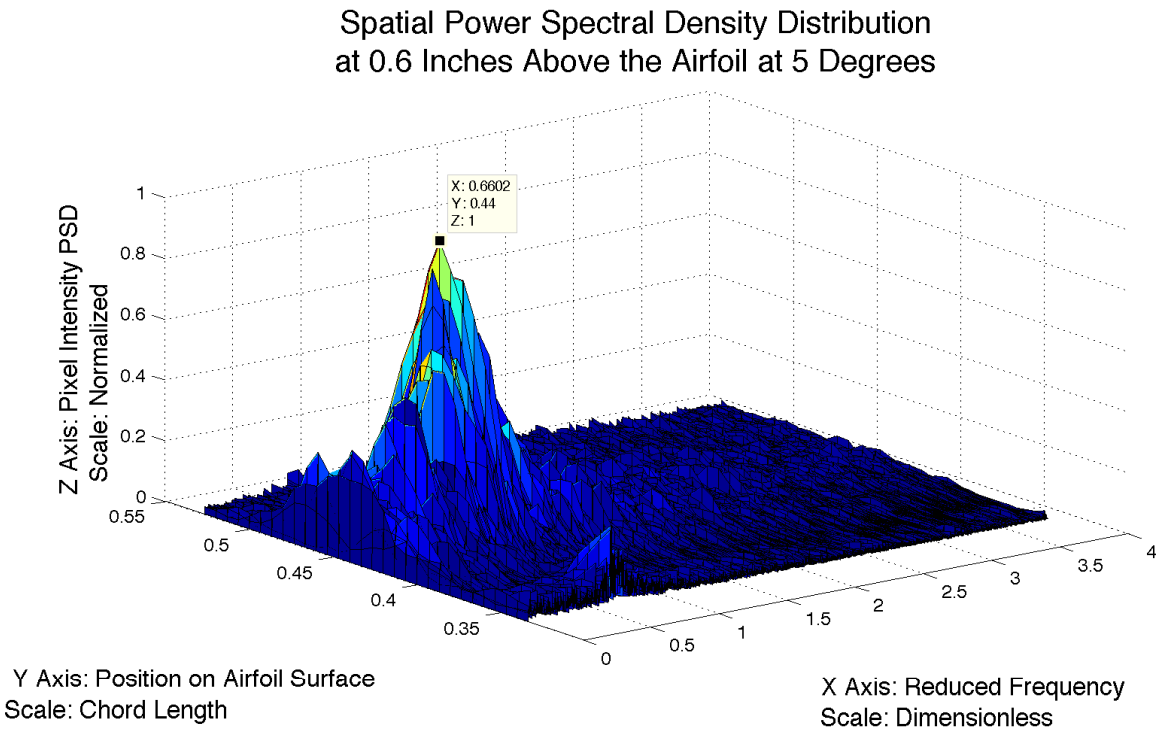

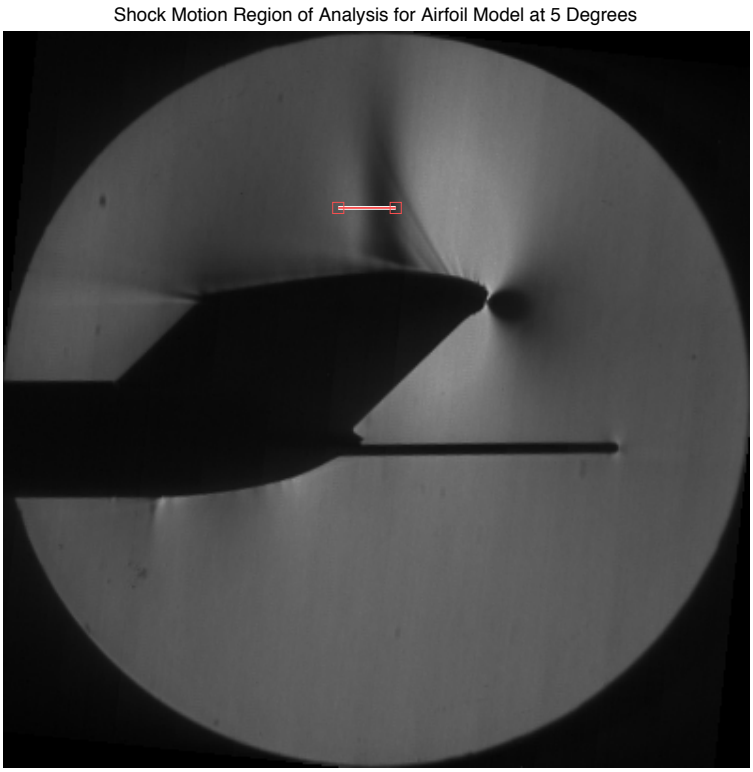

Figure 4.6. Spatial PSD Output (top) and Region of Interest (bottom) for 5° Incidence

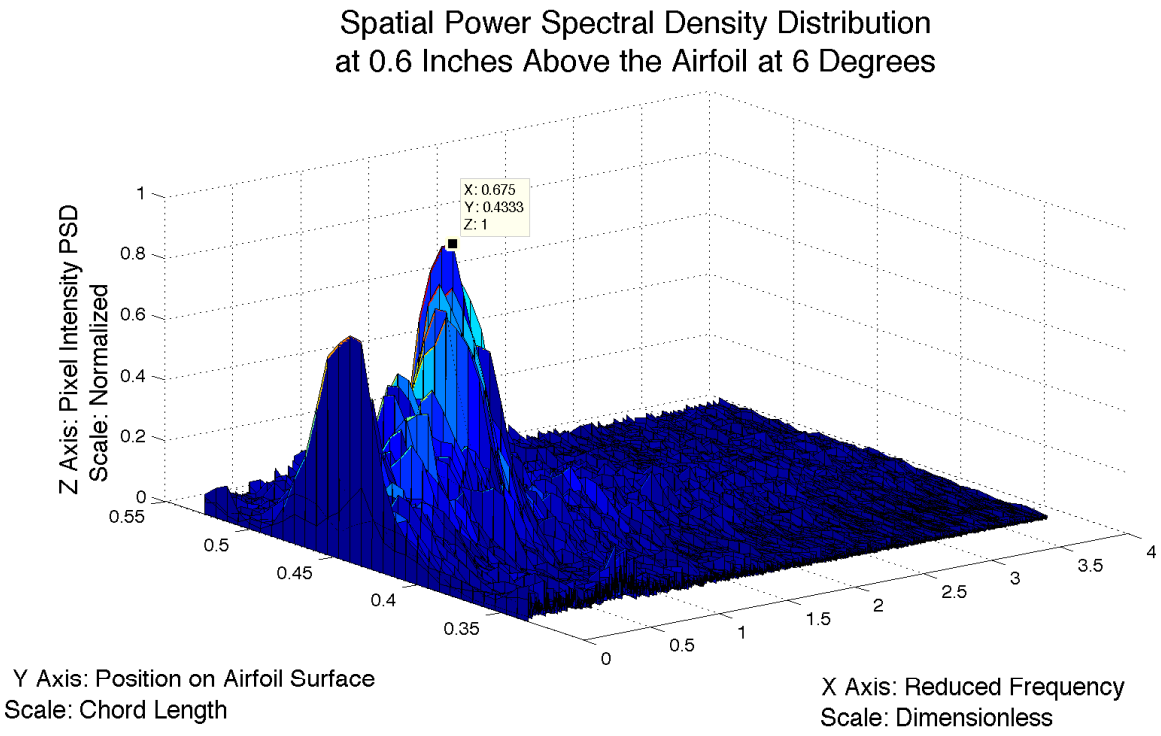

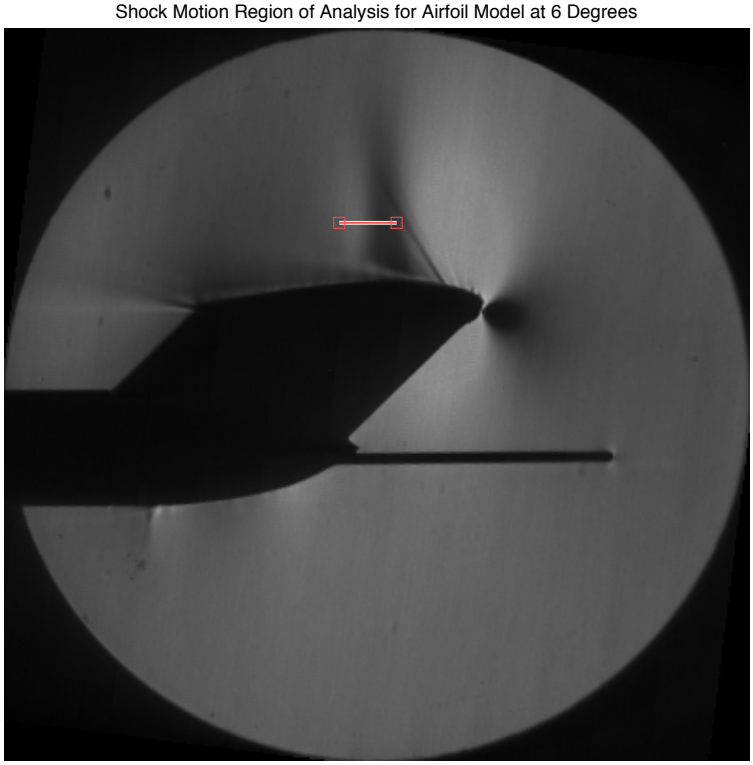

Figure 4.7. Spatial PSD Output (top) and Region of Interest (bottom) for 6° Incidence

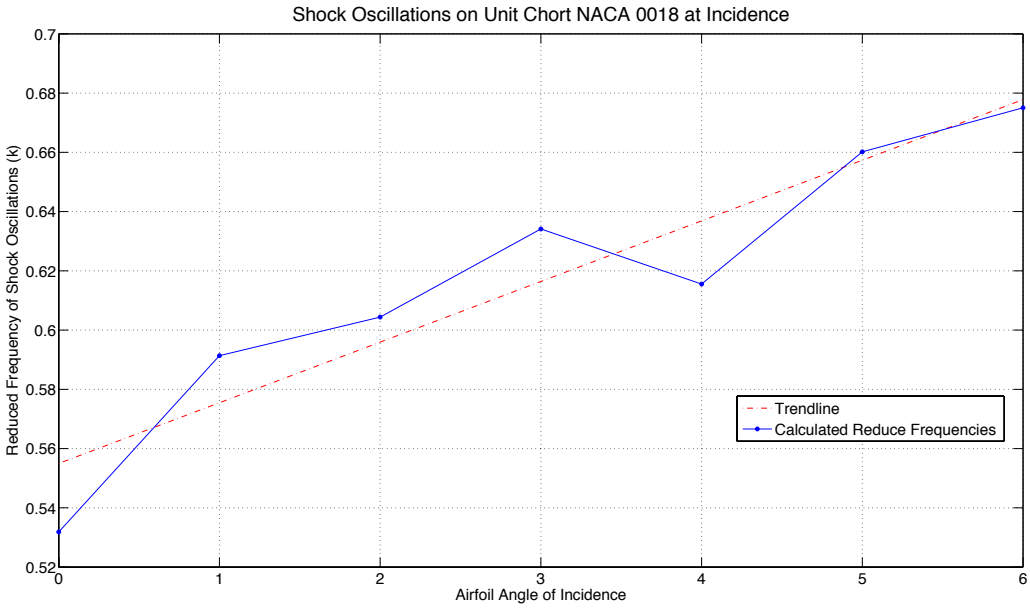

Figure 4.8. Trendline Indicating 0.0205 Reduced Frequency Increase Per Degree Incidence

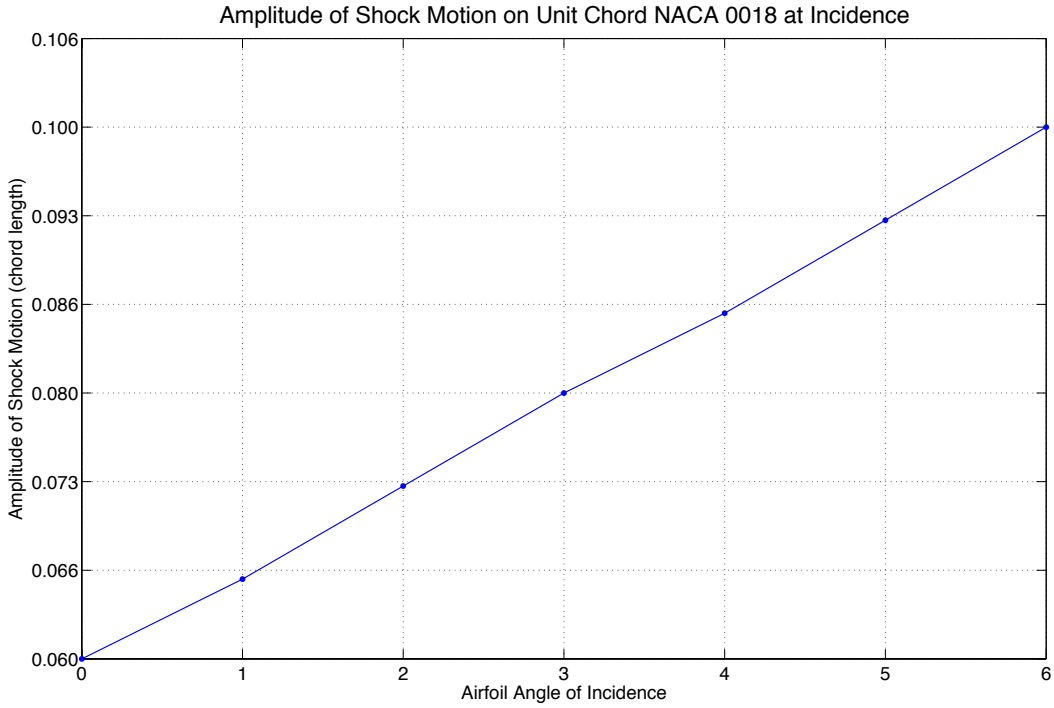

Figure 4.9. Shock Motion Amplitude Increase of 0.0067 Per Degree Incidence

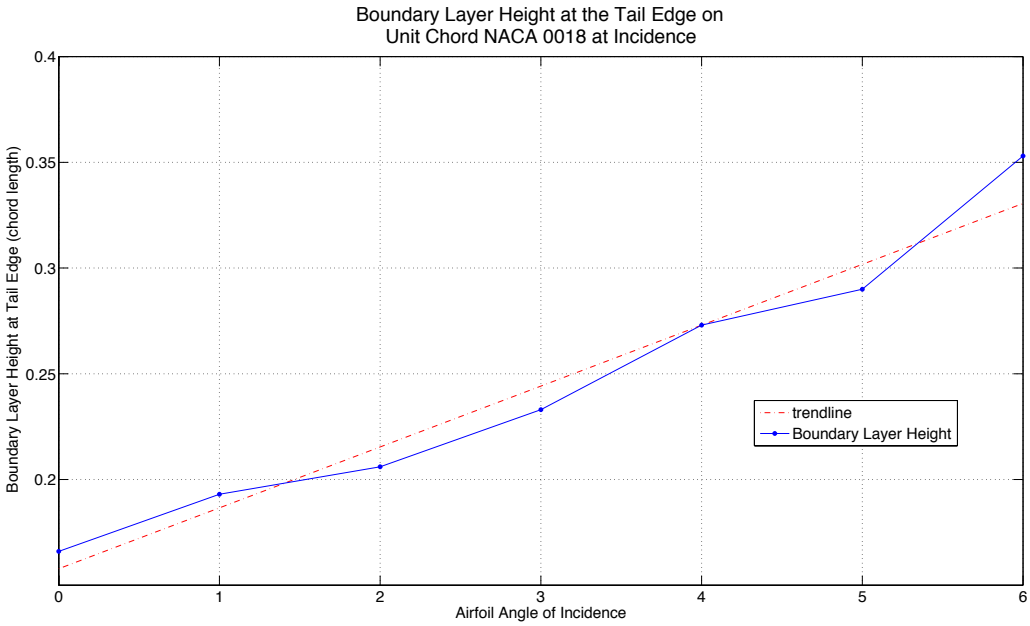

Figure 4.10. Boundary Layer Height Increase by 0.0288 at the Tail Edge Per Degree Incidence

CHAPTER 5
FUTURE WORK

In the present study, a positive correlation was found between angle of incidence and shock oscillation frequency, and a linear trend was extrapolated from this relationship. This study should be extended to examine whether this trend exists across different types of airfoils. The lack of available information regarding the buffeting behavior of the specific airfoil used in this study highlights the need for further understanding of how different airfoils affect buffeting. In particular, studies should be conducted to formulate a more detailed relationship between buffeting behavior and airfoil shape and thickness.

The spatial PSD distribution algorithm could potentially yield better precision when tested with different schlieren sensitivities. Lowering the schlieren sensitivity should minimize the noise due to turbulent flow structures without negatively affecting the visibility of the shock. In addition, the methodology of locating the shock on which the six initial algorithms were based could potentially be more effective if used with other imaging techniques such as PIV, which has been suggested to be more effective at locating precise shock positions than schlieren (Hartmann *et al.*, 2012).

Though it was not the primary purpose of the present study, the spatial PSD distribution algorithm was also applied at the tail edge of the airfoil to examine the boundary layer fluctuations. A good correlation was not found between the frequencies in the wake and the shock oscillation, most likely due to turbulence noise skewing the pixel intensity. This could possibly be avoided by adjusting the schlieren sensitivity and performing the experiment again. Results regarding the tail edge are presented in Appendix A.

The work in the present study has been shown to be a useful way to measure shock oscillations, but to further understand buffeting, it would be valuable to correlate this data

with pressure information. The model design used for the present study could easily be modified to include pressure sensors. Fig. 5.1 shows a proposed schematic of how pressure sensors could be placed onto the model.

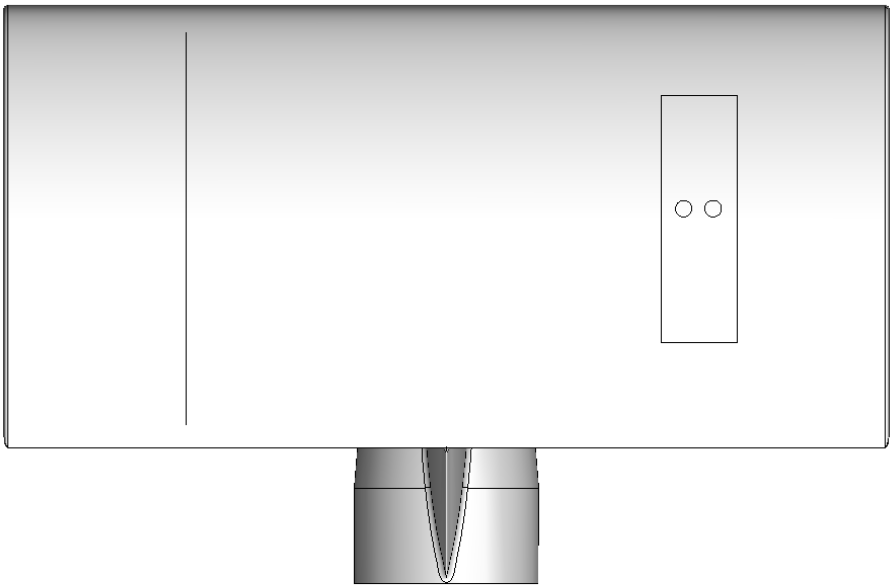

Figure 5.1. Proposed Pressure Sensor Arrangement

The line on the left side of the diagram represents a series of static pressure ports that could span the top and bottom of the airfoil. Data from these sensors could be correlated with the shock motion seen in the schlieren and could offer insights into the unsteady pressure field and behavior of buffeting. The box on the right with the two circles inside it exemplifies a removable section that could house two dynamic pressure transducers, with one sensor facing up and the other facing down. This removable section would make it relatively cheap and easy to reposition the sensors without having to build an entirely new model. This design could be used to test a variety of different airfoils with minimal modification to the overall setup, which would considerably reduce time spent on design and implementation.

BIBLIOGRAPHY

BIBLIOGRAPHY

3D-Systems (2006) *Accura 60 Plastic Data Sheet*. Valencia, CA.

Anderson, J. D. (2001) *Fundamentals of aerodynamics*. McGraw-Hill, Boston.

Barakos, G. & Drikakis, D. (2000) "Numerical simulation of transonic buffet flows using various turbulence closures." *The International journal of heat and fluid flow.*, Vol. 21(5), pp. 620–626.

Becker, J. V. (1980) *The high-speed frontier : case histories of four NACA programs, 1920-1950*. Scientific and Technical Information Branch, National Aeronautics and Space Administration, Washington, D.C.

Benard, E.; Huang, J.-C.; & Raghunathan, S. (2010) "Experimental investigation of unsteadiness in transonic shock boundary layer interaction.".

Bendat, J. & Piersol, A. (2000) *Random Data: Analysis and Measurement Procedures*. John Wiley & Sons, Inc., 3rd edition.

Brentner, K. S.; Lyrintzis, A. S.; & Koutsavdis, E. K. (1997) "Comparison of Computational Aeroacoustic Prediction Methods for Transonic Rotor Noise." *Journal of aircraft.*, Vol. 34(4), pp. 531.

Bruce, P. J. K. & Babinsky, H. (2010) "An experimental study of transonic shock/boundary layer interactions subject to downstream pressure perturbations." *Aerospace Science and Technology Aerospace Science and Technology*, Vol. 14(2), pp. 134–142.

Capone, F. J. (1995) *The NASA Langley 16-foot transonic tunnel historical overview, facility description, calibration, flow characteristics, and test capabilities*. National Aeronautics and Space Administration, Langley Research Center ; National Technical Information Service, distributor, Hampton, Va.; Springfield, Va.

Chen, C.-L. (1985) *Numerical study of porous airfoils in transonic flow*. National Aeronautics and Space Administration, Ames Research Center, Moffett Field, Calif.; Springfield, Va.

Chen, L. W.; Xu, C. Y.; & Lu, X. Y. (2010) "Numerical investigation of the compressible flow past an aerofoil." *Journal of Fluid Mechanics*, Vol. 643, pp. 97–126.

Chew, W. L. (1953) *Wind tunnel investigations of transonic test sections. phase i. tests of a 22.5-percent open-area perforated-wall test section in conjunction with a sonic nozzle.*. Defense Technical Information Center, Ft. Belvoir.

Crouch, J. D.; Garbaruk, A.; Magidov, D.; & Travin, A. (2009) "Origin of transonic buffet on aerofoils." *J.Fluid Mech.Journal of Fluid Mechanics*, Vol. 628, pp. 357–369.

Cunningham, A. M. & Spragle, G. S. (1987) *A study of the effects of Reynolds number and mach number on constant pressure coefficient jump for shock-induced trailing-edge separation*. National Aeronautics and Space Administration, Scientific and Technical Information Office, [Washington, DC]; Springfield, Va.

DeAngelis, V. M. & Monaghan, R. C. (1977) *Buffet characteristics of the F-8 supercritical wing airplane*. National Aeronautics and Space Administration, Scientific and Technical Information Office, [Washington]; Springfield, Va.

Deiwert, G. S.; McDevitt, J. B.; & Levy, L. L. (1976) "Simulation of turbulent transonic separated flow.".

Delery, J.; Marvin, J. G.; Reshotko, E.; for Aerospace Research, N. A. T. O. A. G.; & Panel., D. F. D. (1986) *Shock-wave boundary layer interactions*. NATO, Advisory Group for Aerospace Research and Development ; NTIS, Neuilly sur Seine, France; Springfield, Va.

Despre, C.; Caruana, D.; Mignosi, A.; Reberga, O.; & Correge, M. (2001) *Buffet Active Control - Experimental and Numerical Results.*. Defense Technical Information Center, Ft. Belvoir.

Djavareshkian, M. H. & Islami, S. B. (2004) "Transonic Turbulent Flow Simulation Using Pressure-Based Method And Normalized Variable Diagram." *INTERNATIONAL JOURNAL OF ENGINEERING TRANSACTIONS B*, Vol. 17(3), pp. 297–308.

Doerffer, P. & Szulc, O. (2006) "Shock wave smearing by wall perforation." *Archives of mechanics.Archiwum mechaniki stosowanej.*, Vol. 58(6), pp. 543.

Drela, M. (1986) *Two-dimensional transonic aerodynamic design and analysis using the Euler equations*. Gas Turbine Laboratory, Massachusetts Institute of Technology, Cambridge, Mass.

Dupont, P.; Haddad, C.; & Debiave, J. F. (2006) "Space and time organization in a shock-induced separated boundary layer." *Journal of Fluid Mechanics*, Vol. 559(1), pp. 255–277.

Dussauge, J.-P. & Piponniau, S. (2008) "Shock/boundary-layer interactions: Possible sources of unsteadiness." *J.Fluids Struct.Journal of Fluids and Structures*, Vol. 24(8), pp. 1166–1175.

Edwards, J. W. (1996) *Transonic shock oscillations and wing flutter calculated with an interactive boundary layer coupling method*. National Aeronautics and Space Administration, Langley Research Center ; National Technical Information Service, distributor, Hampton, Va.; Springfield, Va.

Elsenaar, A.; Binion, T. W. J.; Stanewsky, E.; & Hornung, H. G. (1988) *Reynolds number effects in transonic flow*. AGARD, Neuilly sur Seine, France.

Erickson, L. L. (1974) "Transonic single-mode flutter and buffet of a low aspect ratio wing having a subsonic airfoil shape.".

Ewald, B. F. R.; for Aerospace Research, N. A. T. O. A. G.; & Panel., D. F. D. (1998) *Wind tunnel wall correction = la Correction des effets de paroi en soufflerie*. AGARD, North Atlantic Treaty Organization ; [Available from] NASA Center for Aerospace Information, Neuilly-sur-Seine Cedex, France; Hanover, MD.

Harris, C. D. (1990) "NASA supercritical airfoils a matrix of family-related airfoils.".

Hartmann, A.; Klaas, M.; & Schroder, W. (2012) "Time-resolved stereo PIV measurements of shock-boundary layer interaction on a supercritical airfoil." *Experiments in Fluids*, Vol. 52(3), pp. 591–604.

Hilton, W. F. & Fowler, R. G. (1952) *Photographs of shock wave movement*. HMSO, London.

Humphreys, M. D. (1951) *Pressure pulsations on rigid airfoils at transonic speeds*. National Advisory Committee for Aeronautics, Washington, D.C.

Jacobs, E. N.; Ward, K. E.; & Pinkerton, R. M. (1935) *The characteristics of 78 related airfoil sections from tests in the variable-density wind tunnel*. NASA Langley Research Center, Hampton, Va.

Johnson, D. A. & Bachalo, W. D. (1980) "Transonic Flow Past a Symmetrical Airfoil-Inviscid and Turbulent Flow Properties." *AIAA J AIAA Journal*, Vol. 18(1), pp. 16–24.

Johnson, D. A.; Bachalo, W. D.; & Owen, F. K. (1981) "Transonic Flow Past a Symmetrical Airfoil at High Angle of Attack." *J Aircraft Journal of Aircraft*, Vol. 18(1), pp. 7–14.

Kim, H.-D.; Hong, J.-W.; & Matsuo, K. (1993) "Criterion of Turbulent Boundary-Layer Separation Induced by Shock-Wave.".

Krynytzky, A. J. (2001) "Steady-State Wall Interference of a Symmetric Half-Model in the Langley Transonic Dynamics Tunnel.".

Lee, B. H. K. (1984) *A study of transonic flutter of a two-dimensional airfoil using the U-g and p-k methods*. National Research Council Canada, Ottawa.

Lee, B. H. K. (2001) "Self-sustained shock oscillations on airfoils at transonic speeds." *Progress in Aerospace Sciences*, Vol. 37(2), pp. 147–196.

Lee, B. H. K. (2002) "Statistical analysis of wing/fin buffeting response." *Progress in Aerospace Sciences*, Vol. 38(4-5), pp. 305–345.

Lee, B. H. K. & Tang, F. C. (1988) *An experimental study of transonic buffet of a supercritical airfoil with trailing edge flap.* NAE Publications Section, Ottawa, Ont.

Levy, L. L. (1978) "Experimental and Computational Steady and Unsteady Transonic Flows about a Thick Airfoil." *AIAA J AIAA Journal*, Vol. 16(6), pp. 564–572.

Lockheed-Martin (2002) *High Speed Wind Tunnel and Test Systems Design Handbook.* Lockheed Martin, Dallas, TX.

Marvin, J. G.; Levy, L. L.; & Seegmiller, H. L. (1980) "Turbulence Modeling for Unsteady Transonic Flows." *AIAA J AIAA Journal*, Vol. 18(5), pp. 489–496.

Mason, W. H. (2006) "Configuration Aerodynamics.".

McDevitt, J. B. & Okuno, A. F. (1985) *Static and dynamic pressure measurements on a NACA 0012 airfoil in the Ames High Reynolds Number Facility.* National Aeronautics and Space Administration, Scientific and Technical Information Branch, [Washington, DC]; Springfield, Va.

Mercer, J. E.; Geller, E. W.; Jameson, A.; & Johnson, M. L. (1981) "Transonic Flow Calculations for a Wing in a Wind Tunnel." *Journal of Aircraft*, Vol. 18(9), pp. 707–711.

Mokry, M.; Khalid, M.; & Mebarki, Y. (2000) "The Art and Science of Wind Tunnel Wall Interference: New Challenges, Abstract for the 22nd ICAS Congress..".

Morgans, A.; Karabasov, S.; Dowling, A.; & Hynes, T. (2003) "Transonic Helicopter Noise." *Annual forum proceedings.*, Vol. 59, pp. 46–55.

Nelson, T. E. & Zingg, D. W. (2004) "Fifty Years of Aerodynamics: Successes, Challenges, and Opportunities." *Canadian Aeronautics and Space Journal*, Vol. 50, pp. 61–84.

Ngoc, H. T. B. & Hung, N. M. (2011) "Study of separation phenomenon in transonic flows produced by interaction between shock wave and boundary layer." *Vietnom Journal of Mechanics*, Vol. 33(3), pp. 170–181.

Pearcey, H. H. (1959) *Some effects of shock-induced separation of turbulent boundary layers in transonic flow past aerofoils.* H.M.S.O., London.

Pearcey, H. H. & Holder, D. W. (1967) *Examples of the effects of shock-induce boundary-layer separation in transonic flight,.* H.M.S.O., London.

Prananta, B. B. (1999) *Physical and numerical aspects of aeroelastic simulations*. Netherlands.

Pulliam, T. H. & Steger, J. L. (1980) "Implicit Finite-Difference Simulations of Three-Dimensional Compressible Flow." *AIAA J AIAA Journal*, Vol. 18(2), pp. 159–167.

Raghunathan, S.; Gillan, M. A.; Cooper, R. K.; Mitchell, R. D.; & Cole, J. S. (1999) "Shock oscillations on biconvex aerofoils." *Aerospace Science and Technology*, Vol. 3(1), pp. 1–10.

Raveh, D. E. & Dowell, E. H. (2011) "Frequency lock-in phenomenon for oscillating airfoils in buffeting flows." *Journal of Fluids and Structures*, Vol. 27(1), pp. 89–104.

Ricketts, R. H. (1983) *Geometric and structural properties of a rectangular supercritical wing oscillated in pitch for measurement of unsteady transonic pressure distributions*. National Aeronautics and Space Administration, Langley Research Center, Hampton, Va.

Rubesin, M. W.; Okuno, A. F.; Levy, L. L.; McDevitt, J. B.; & Seegmiller, H. L. (1976) "An experimental and comutational investigation of the flow field about a transonic airfoil in supercritical flow with turbulent boundary-layer separation.".

Seifert, A. & Pack, L. G. (1999) "Oscillatory Excitation of Unsteady Compressible Flows over Airfoils at Flight Reynolds Numbers.".

Settles, G. S. (2001) *Schlieren and shadowgraph techniques: visualizing phenomena in transparent media*. Springer, Berlin; New York.

Sheldahl, R. E. & Klimas, P. C. (1981) *Aerodynamic characteristics of seven symmetrical airfoil sections through 180-degree angle of attack for use in aerodynamic analysis of vertical axis wind turbines*. Sandia National Laboratories.

Sorenson, R. M.; Wyss, J. A.; & Kyle, J. C. (1951) *Preliminary investigation of the pressure fluctuations in the wakes of two-dimensional wings at low angles of attack*. National Advisory Committee for Aeronautics, Washington, D.C.

Spooner, S. (1931) "Technical Report by the Accidents Investigation Sub-Committee on the accident to the aeroplane G-AAZK at Meopham, Kent, on 21st July, 1930.." *Flight*, Vol. 22(5), pp. 104.

Thiery, M. N. & Coustols, E. (2006) "Numerical prediction of shock induced oscillations over a 2D airfoil: Influence of turbulence modelling and test section walls." *The International journal of heat and fluid flow.*, Vol. 27(4), pp. 661–670.

Thomas, J. P.; Dowell, E. H.; & Hall, K. C. (2002) "Nonlinear Inviscid Aerodynamic Effects on Transonic Divergence, Flutter, and Limit-Cycle Oscillations." *AIAA Journal*, Vol. 40, pp. 638–646.

Tijdeman, H. (1977) *Investigations of the Transonic Flow Around Oscillating Airfoils.* PhD thesis.

Tulita, C.; Raghunathan, S.; & Benard, E. (2004) "Drag reduction and buffeting alleviation in transonic periodic flow over biconvex aerofoils, Abstract for the 24th ICAS Congress..".

Tulita, C.; Turkbeyler, E.; & Raghunathan, S. (1995) "Investigation of the Influence of the Turbulent Transition on the Transonic Periodic Flow.".

Williams, M. H.; Bland, S. R.; & Edwards, J. W. (1985) *Flow instabilities in transonic small disturbance theory.* National Aeronautics and Space Administration, Langley Research Center, Hampton, Va.

Wilmoth, R. G. (1977) *Computation of transonic boattail flow with separation.* National Aeronautics and Space Administration, Scientific and Technical Information Office, [Washington]; Springfield, Va.

Xiao, Q.; Tsai, H. M.; & Liu, F. (2006) "Numerical Study of Transonic Buffet on a Supercritical Airfoil." *AIAA Journal*, Vol. 44(3), pp. 620–663.

Xiong, J.; Nezhad, S. T.; & Liu, F. (2010) "Computation of Self-excited Unsteady Transonic Flow of an Airfoil in a Channel Using URANS and DES; 40th Fluid Dynamics Conference and Exhibit.".

LIST OF APPENDICES

APPENDIX A

APPENDIX A

ADDITIONAL RESULTS

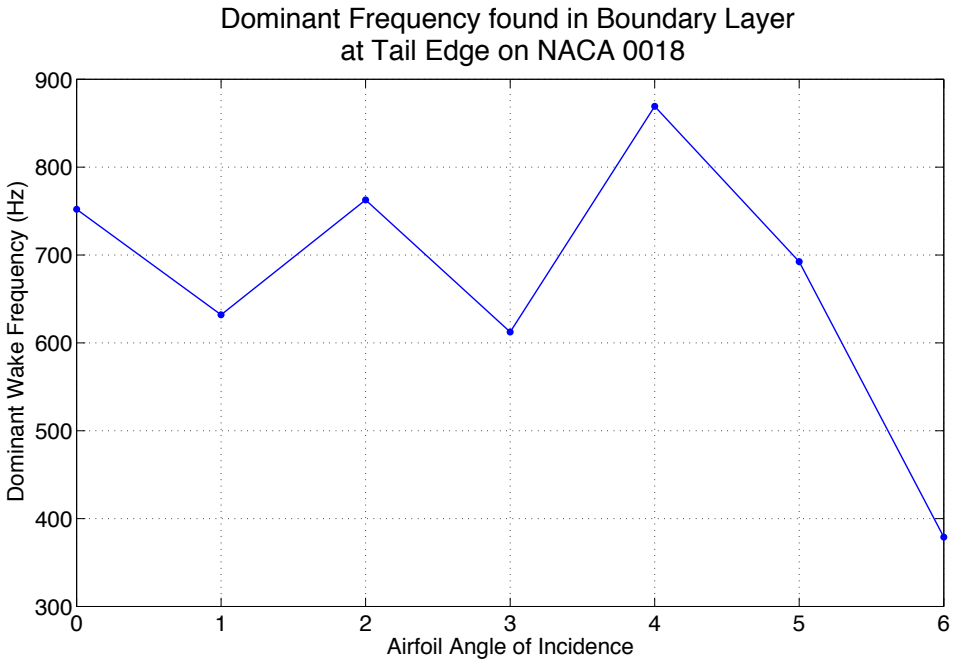

Figure A.1. Dominant Frequencies in the Boundary Layer at the Tail Edge Per Degree Incidence

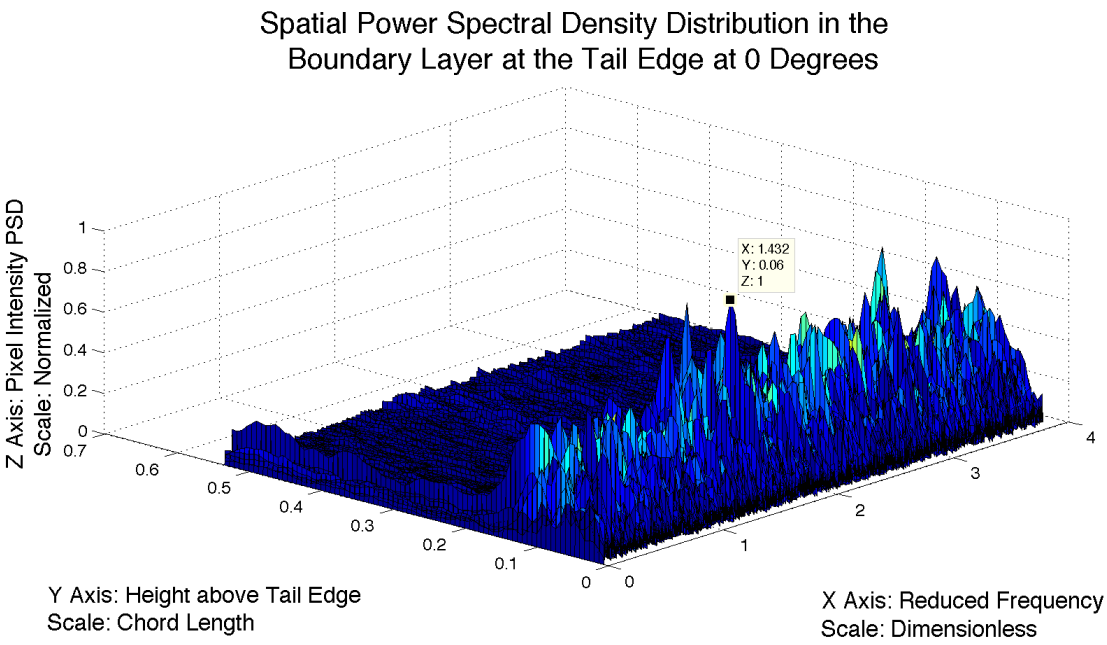

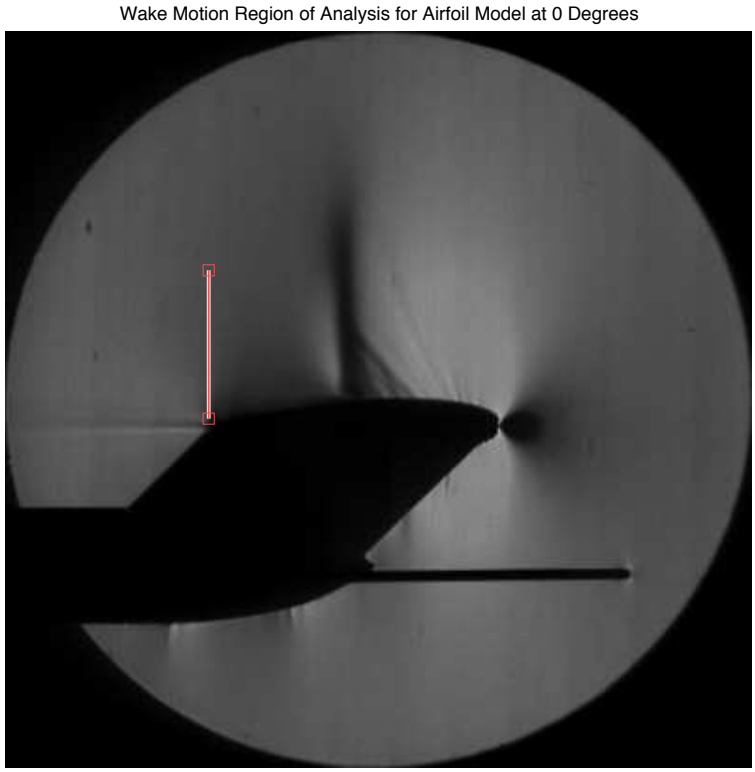

Figure A.2. Spatial PSD Output (top) and Region of Interest (bottom) for 0° Incidence at Tail Edge

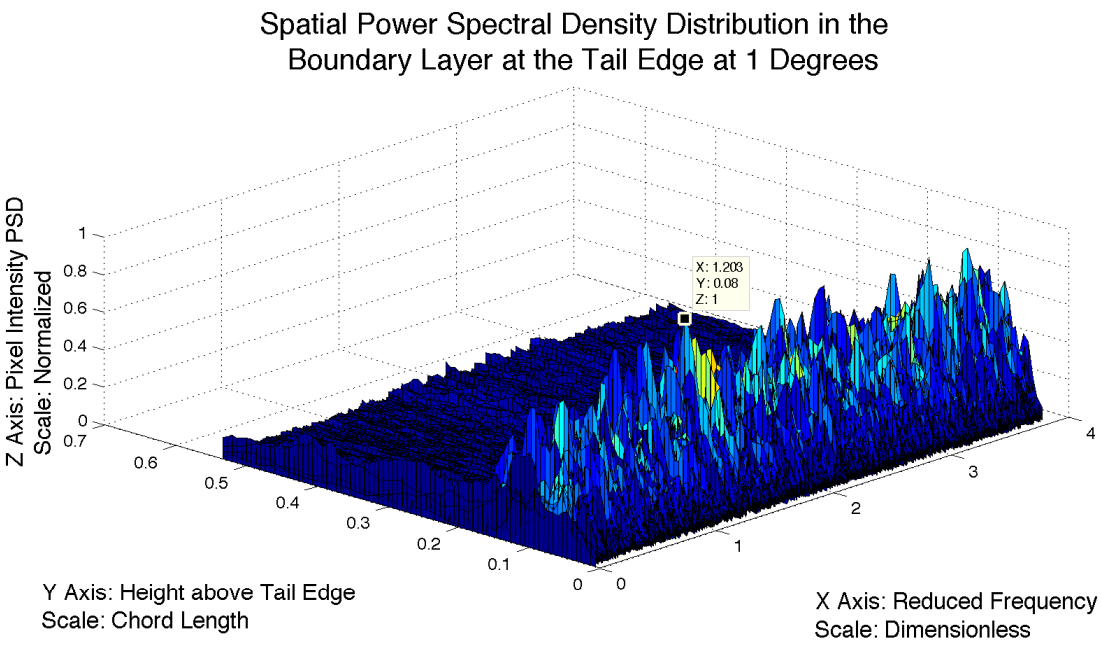

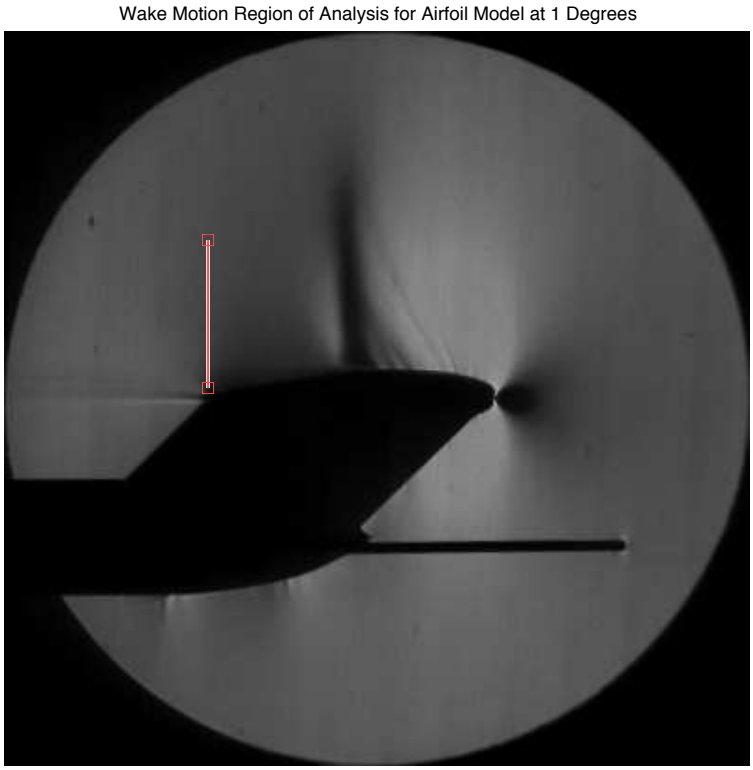

Figure A.3. Spatial PSD Output (top) and Region of Interest (bottom) for 1° Incidence at Tail Edge

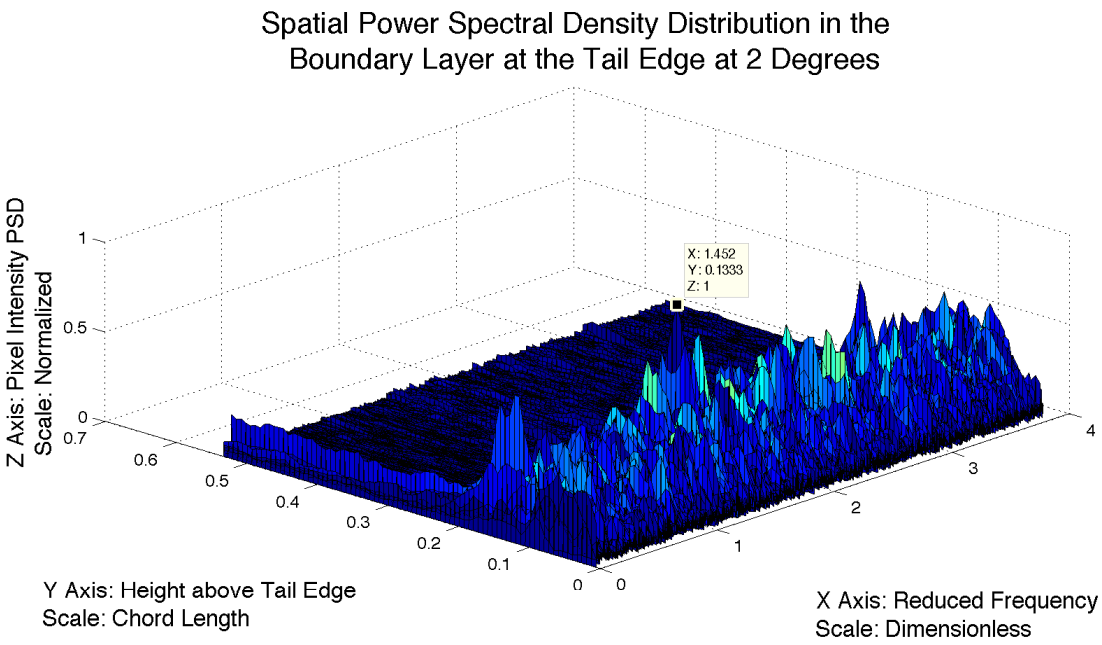

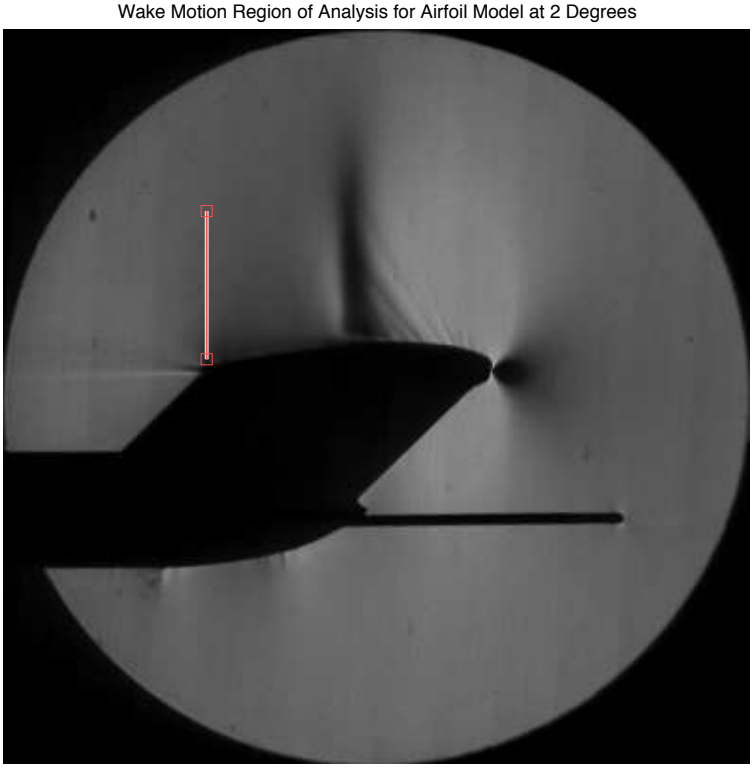

Figure A.4. Spatial PSD Output (top) and Region of Interest (bottom) for 2° Incidence at Tail Edge

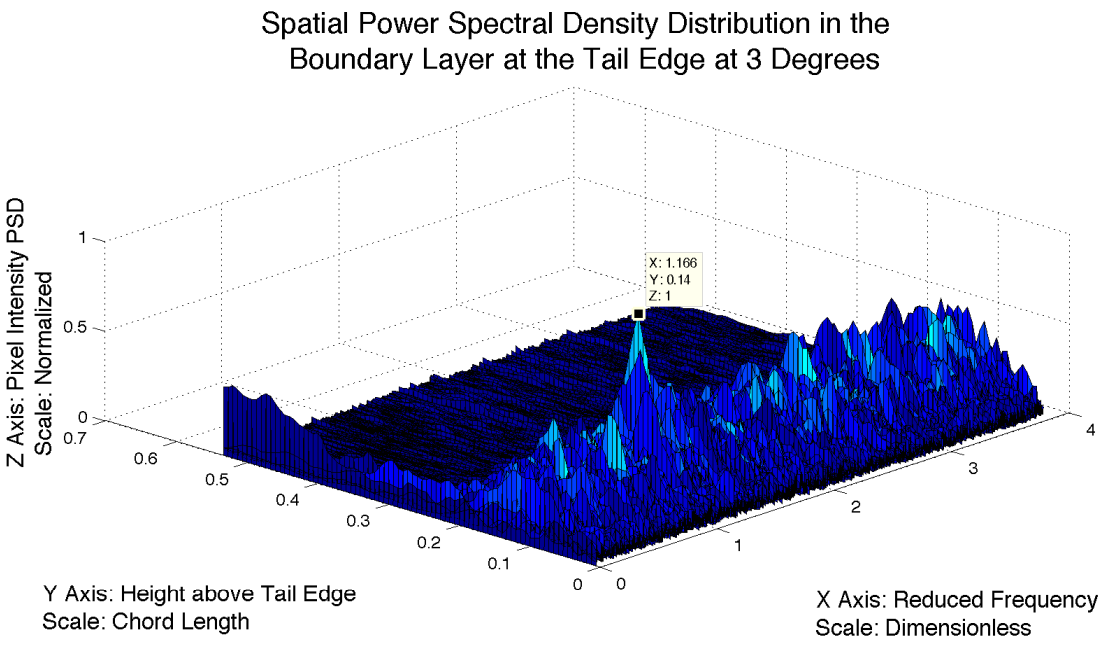

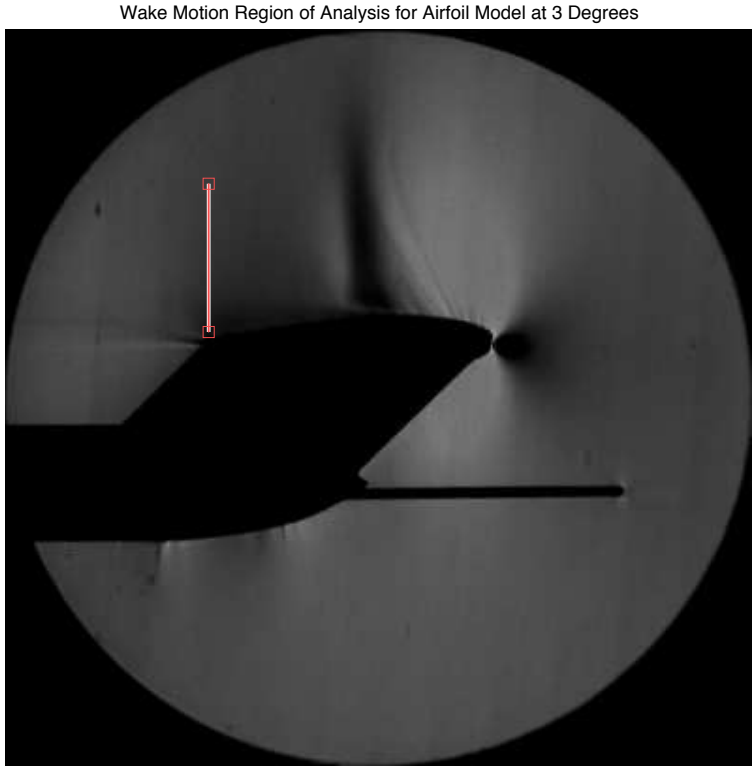

Figure A.5. Spatial PSD Output (top) and Region of Interest (bottom) for 3° Incidence at Tail Edge

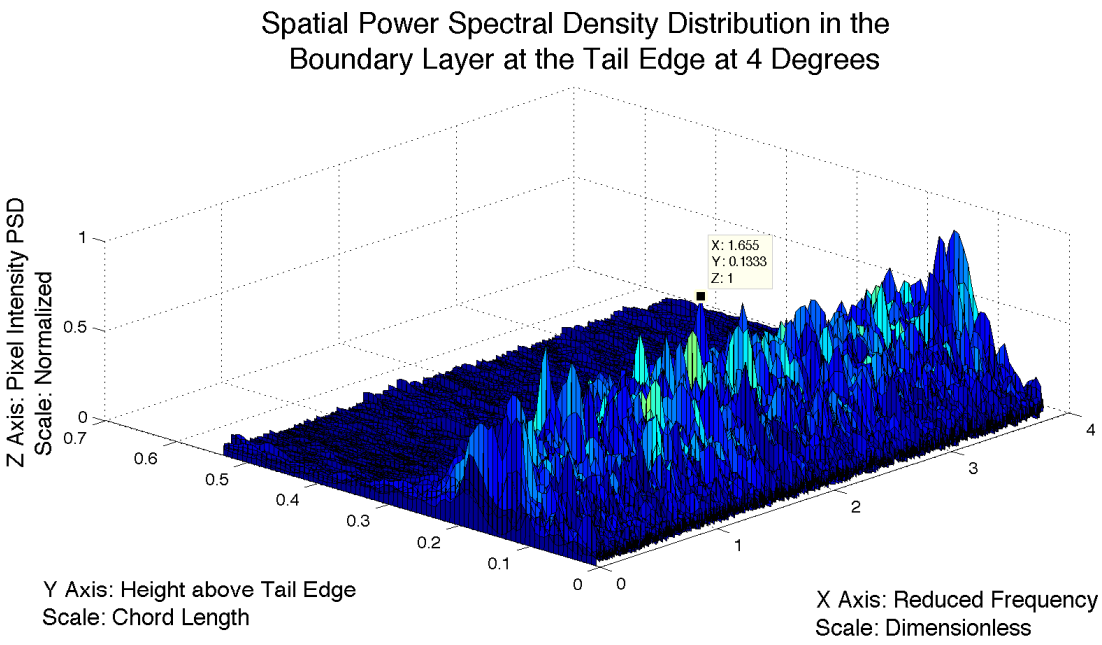

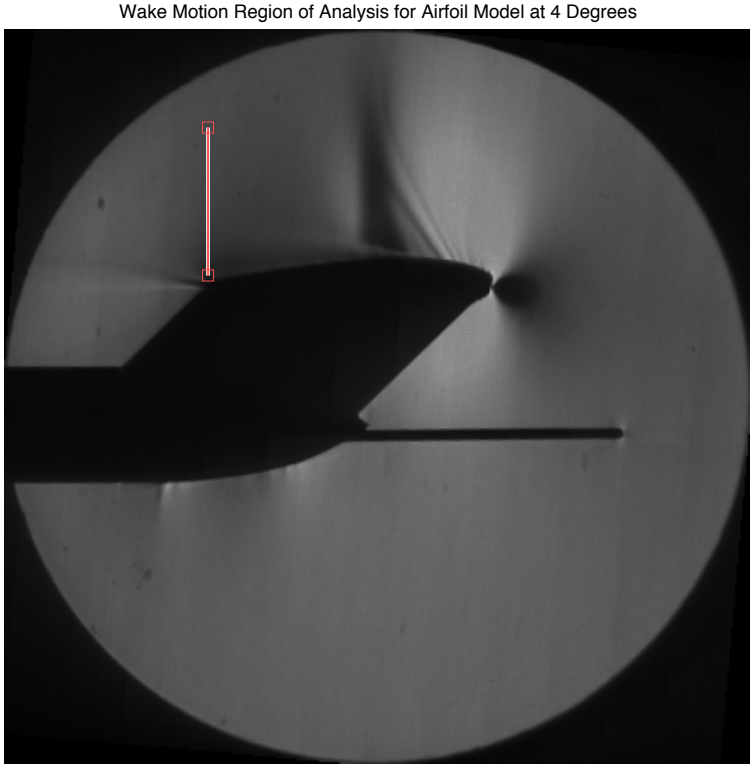

Figure A.6. Spatial PSD Output (top) and Region of Interest (bottom) for 4° Incidence at Tail Edge

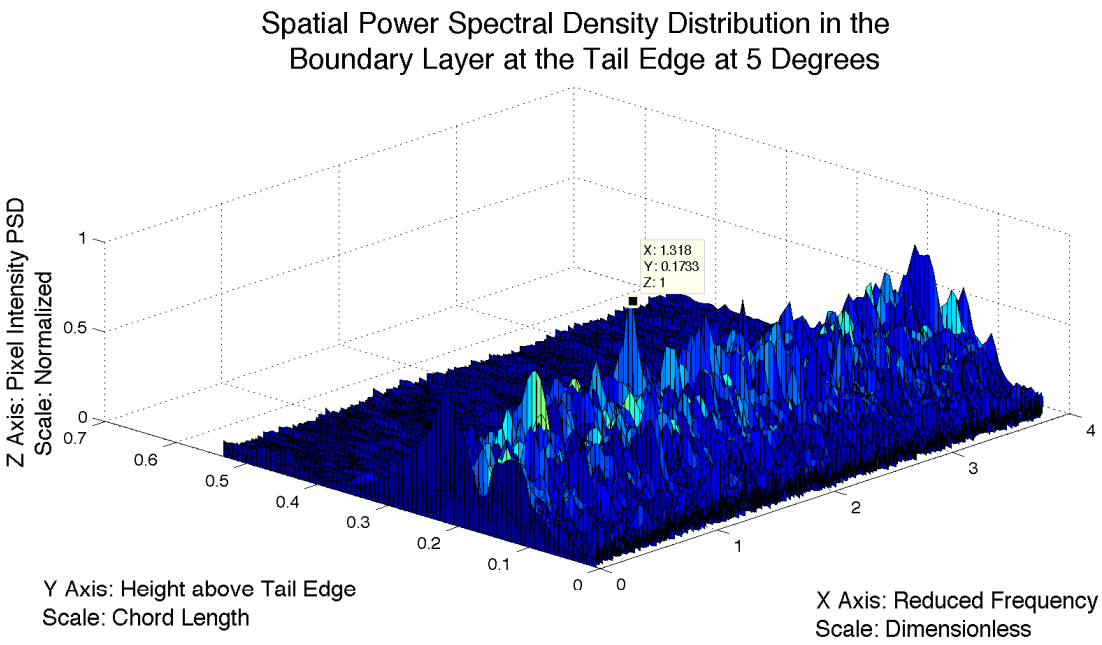

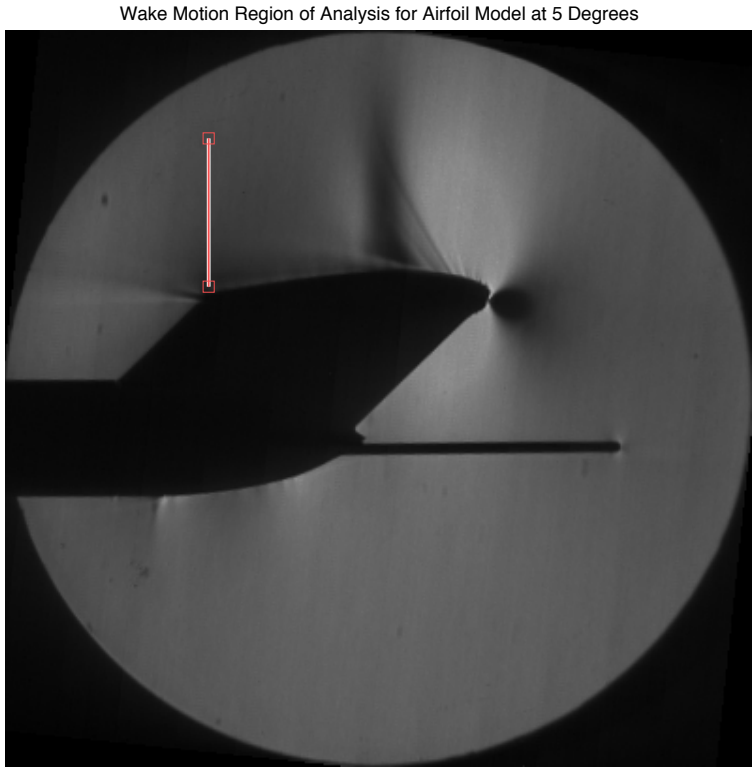

Figure A.7. Spatial PSD Output (top) and Region of Interest (bottom) for 5° Incidence at Tail Edge

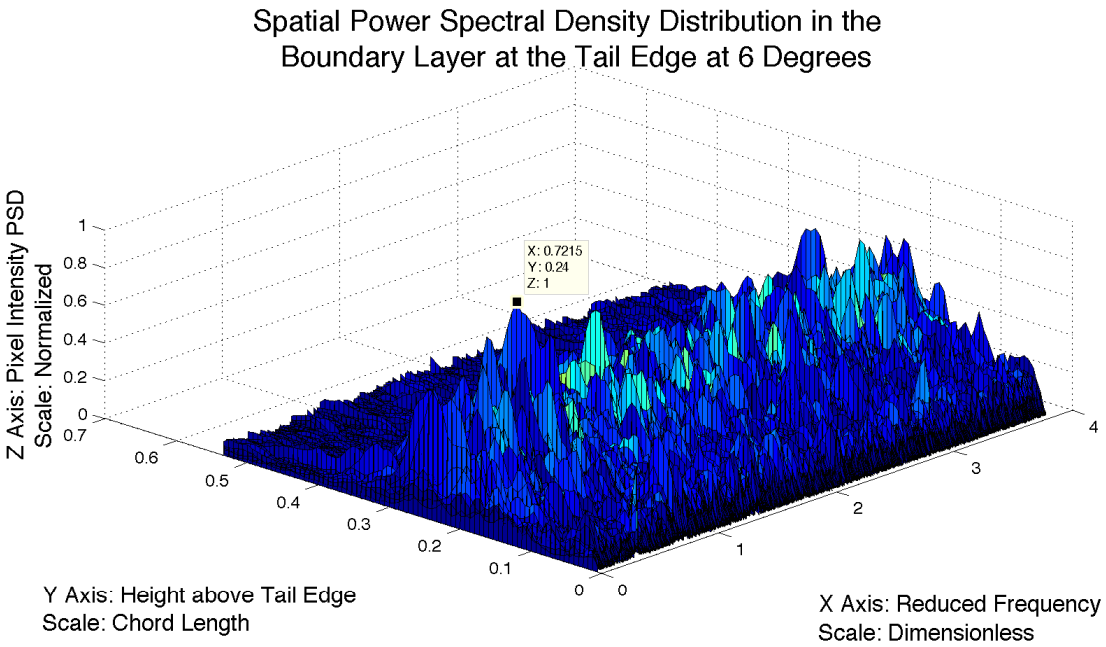

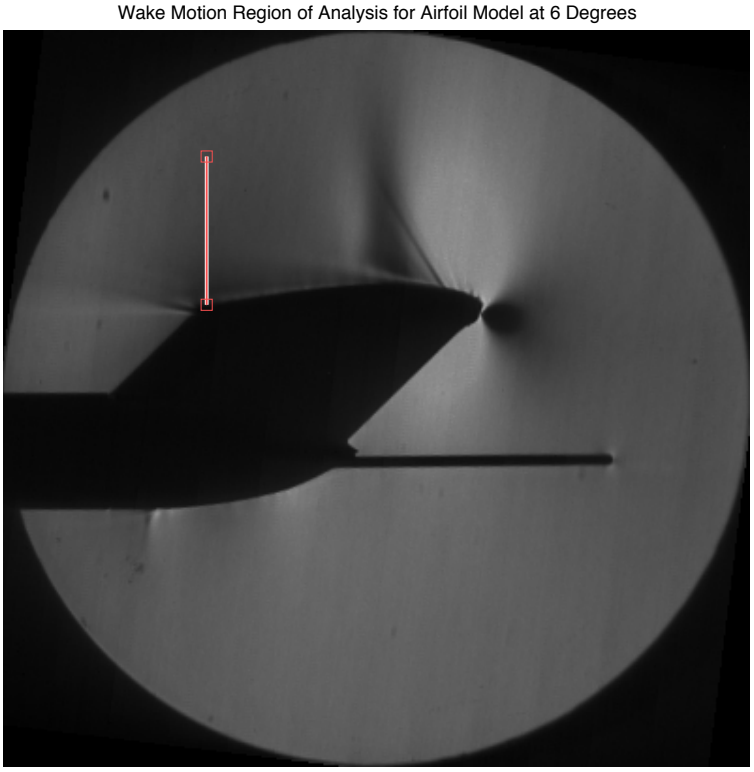

Figure A.8. Spatial PSD Output (top) and Region of Interest (bottom) for 6° Incidence at Tail Edge

APPENDIX B

APPENDIX B

CODE LISTING

```
clear all

close all


%%%%%%%%%%%%%%%%%%%%%%%%%%%%%%%%%%%%%%%%%%%%%%%%%%%%%%%%%%%%%%%%%%%%%%%%%%%%
%Set File Path
for WingAngle = 0:6 %input('Enter wing angle attack:  ');
WingAngle
%Choose a tunnel run & establish reference positions for that set of images
if     WingAngle == 0
    TR     = '78';
    XShock = 180;
    XNose  = 260;
    YMax   = 195;
elseif WingAngle == 1
    TR     = '79';
    XShock = 180;
    XNose  = 260;
    YMax   = 180;
elseif WingAngle == 2
    TR     = '80';
    XShock = 185;
```

```
    XNose  = 260;
    YMax   = 165;
elseif WingAngle == 3
    TR     = '81';
    XShock = 185;
    XNose  = 260;
    YMax   = 150;
elseif WingAngle == 4
    TR     = '86';
    XShock = 190;
    XNose  = 260;
    YMax   = 120;
elseif WingAngle == 5
    TR     = '87';
    XShock = 195;
    XNose  = 260;
    YMax   = 125;
else
    TR     = '88';
    XShock = 195;
    XNose  = 260;
    YMax   = 135;
end %End If
FolderName = strcat('../NCPA/Thesis Data/TR10',TR,'/');

%%%%%%%%%%%%%%%%%%%%%%%%%%%%%%%%%%%%%%%%%%%%%%%%%%%%%%%%%%%%%%%%%%%%%%%%%%%%%%%
```

```
%Declare variables used in the analysis loops
TEHeight  = 80;
NSlices   = 4096;  %input('Enter the number of slices to use: ');
NBlocks   = 3;       %input('Enter the number of time blocks to use: ');
NSlices   = NSlices*NBlocks;
NAPix     = 30;      %input('Enter the pixel array length to analyze: ');
YStart    = 5;         %input('Enter the initial height above wing surface: ');
NSteps    = 1;       %input('Enter the number of analysis arrays to use: ');
StepSize  = 1;       %input('Enter the step size between the analysis arrays: ');
BlockSize = NSlices/NBlocks;
Values    = zeros(BlockSize,NAPix);
Values2   = zeros(BlockSize,TEHeight);
PSDGxx    = zeros(NAPix,BlockSize/2,NBlocks);
Line      = zeros(NSteps+1, 4);

%Define frequency scaling based on sampling rate
PSDdel_f = (4000/BlockSize)*(1:BlockSize/2);

%Loop for analyzing shock motion in each selected ROI
for step = 0:NSteps-1

    %Reset time-block for selected ROI
    InitImage=0;

    %Loop for processing each time-block
    for b = 1:NBlocks
```

```
%Loop for reading in ROI from each image
for image = InitImage+1:BlockSize*b
    %Read in time-slice image
    FileName = strcat('TR10',TR,'_',num2str(image),'.tif');
    Slice    = double(imadjust(imread(strcat...
        (FolderName,FileName))));
    %Invert the image and scale the pixel intensity
    Slice = ((-1)*(Slice-max(max(Slice))));
    %Read in ROI for spectral analysis
    x = image - InitImage;
    [Values(x,1:NAPix),Line(step+1,1:4)] = imcrop(Slice,...
            [XShock-NAPix/2,YMax-YStart-StepSize*step,NAPix-1,0]);
end %End For-3

%Perform FFT on each pixel in the selected ROI
for y = 1:NAPix
    %Remove the mean from the time series data and perform FFT
    X  = Values(1:BlockSize,y)-mean(Values(1:BlockSize,y));
    XL = length(X);
    Xk = fft(X);
    %Calculate two-sided PSD
    PSDSxx = (1/XL)^2*(conj(Xk).*Xk);
    %Calculate one-sided PSD
    PSDGxx(y,1:XL/2,b) = 2*PSDSxx(1:XL/2);
end %End For-4
```

```
    %Adjust starting image to the next time-block
    InitImage = BlockSize*b;

end %End For-2

%Plot spatial PSD distribution for current ROI
figure;
if (NBlocks==1)
    surf(2*pi*.25*PSDdel_f/(1130*.73),...
        (XNose-(XShock-NAPix/2+(NAPix:-1:1)))/150,...
        flipud(PSDGxx(:,:,b))/max(max(flipud(PSDGxx(:,:,b)))));
else
    surf(2*pi*.25*PSDdel_f/(1130*.73),...
        (XNose-(XShock-NAPix/2+(NAPix:-1:1)))/150,...
        flipud(mean(PSDGxx,3))/max(max(flipud(mean(PSDGxx,3)))));
end %End If
title (strcat(['Spatial Power Spectral Density Distribution at ',...
    num2str((StepSize*step+YStart)*.02),' Inches Above the Wing']));
xlabel(char('X Axis: Reduced Frequency','Scale: Dimensionless'));
ylabel(char('Y Axis: Position on Airfoil Surface     ',...
    'Scale: Fraction of Chord Length'));
zlabel(char('Z Axis: Pixel Intensity PSD','Scale: Normalized'));
if (step==0)
    saveas(gcf,strcat('../NCPA/Masters Thesis/ThesisImages/',...
        'Chap3Images/',num2str(WingAngle),'deglower.fig'))
```

```
    else
        saveas(gcf,strcat('../NCPA/Masters Thesis/ThesisImages/',...
            'Chap3Images/',num2str(WingAngle),'degupper.fig'))
    end %End If

    %Print maximum shock motion frequency for current ROI
    PSDdel_f(max(mean(PSDGxx,3)==max(max(mean(PSDGxx,3)))))

end %End For-1

%Reset time-block for analyzing wake motion
InitImage=0;
%Loop for analyzing wake motion
for b = 1:NBlocks

    %Loop for reading in wake ROI
    for image = InitImage+1:BlockSize*b
        %Read in time-slice image
        FileName = strcat('TR10',TR,'_',num2str(image),'.tif');
        Slice    = double(imadjust(imread(strcat(FolderName,FileName))));
        %Invert the image and scale the pixel intensity
        Slice = ((-1)*(Slice-max(max(Slice))));
        %Read in ROI for spectral analysis
        x = image - InitImage;
        [Values2(x,1:TEHeight),Line(NSteps+1,1:4)] = ...
            imcrop(Slice,[110,YMax+13-TEHeight,0,TEHeight-1]);
```

```
    end %End For-2

    %Perform FFT on each pixel in the selected ROI
    for y = 1:TEHeight
        %Remove the mean from the time series data and perform a FFT
        X  = Values2(1:BlockSize,y)-mean(Values2(1:BlockSize,y));
        XL = length(X);
        Xk = fft(X);
        %Calculate two-sided PSD
        PSDSxx = (1/XL)^2*(conj(Xk).*Xk);
        %Calculate one-sided PSD
        PSDGxx(y,1:XL/2,b) = 2*PSDSxx(1:XL/2);
    end %End For-3

    %Adjust starting image to the next time-block
    InitImage = BlockSize*b;

end %End For-1

%Plot spatial PSD distribution for wake ROI
figure;
if (NBlocks==1)
    surf(2*pi*.25*PSDdel_f/(1130*.73),(1:TEHeight)/150,...
        flipud(PSDGxx(:,:,b))/max(max(flipud(PSDGxx(:,:,b)))));
else
    surf(2*pi*.25*PSDdel_f/(1130*.73),(1:TEHeight)/150,...
```

```
        flipud(mean(PSDGxx,3))/max(max(flipud(mean(PSDGxx,3)))));
end %End If
title (strcat(['Spatial Power Spectral Density Distribution above '...
    'the Tail Edge']));
    xlabel(char('X Axis: Reduced Frequency','Scale: Dimensionless'));
ylabel(char('Y Axis: Height above Tail Edge   ',...
    'Scale: Fraction of Chord Length'));
    zlabel(char('Z Axis: Pixel Intensity PSD','Scale: Normalized'));
saveas(gcf,strcat('../NCPA/Masters Thesis/ThesisImages/Chap3Images/'...
    ,num2str(WingAngle),'degwake.fig'))
%Print maximum wake frequency
PSDdel_f(max(mean(PSDGxx,3)==max(max(mean(PSDGxx,3)))))

%Display image showing analysis regions
SliceAve   = strcat(FolderName,'TR10',TR,'_0ave.tif');
figure; imshow(SliceAve)
%Loop for drawing lines for each ROI
for step = 0:NSteps-1
    %Plot lines on image ROIs
    imline(gca,[Line(step+1,1) Line(step+1,1)+Line(step+1,3)],...
        [Line(step+1,2) Line(step+1,2)+Line(step+1,4)]);
    imline(gca,[Line(NSteps+1,1) Line(NSteps+1,1)+Line(NSteps+1,3)],...
        [Line(NSteps+1,2) Line(NSteps+1,2)+Line(NSteps+1,4)]);
    title(strcat(['Shock & Wake Motion Regions of Analysis for'...
        'Airfoil Model at ',num2str(WingAngle),' Degrees']));
    saveas(gcf,strcat('../NCPA/Masters Thesis/ThesisImages/Chap3Images/',...
```

```
        num2str(WingAngle),'deglines.fig'))
end %End For


end %End "Main" For
```

VITA

Second Lieutenant Christopher Farrell was born in Greenwood, Mississippi. He is an only child and was raised by a single mother, Doris Farrell. He graduated from Greenwood High School with honors in 1997, and then went on to complete a Bachelor of Science in Engineering with an emphasis in Biological Engineering at Mississippi State University in 2004. Following that degree, Farrell met his soon-to-be wife Rachel Goodwiller, who became Rachel Farrell in April 2006. They started a concierge business together in Oxford, Mississippi in the summer of 2007, which they ran until June 2008 when Farrell enlisted in the Army National Guard as an Air Traffic Controller. He finished Air Traffic Control training at the top of his class in May 2009. The following August, Farrell decided to pursue a Master of Science in Engineering with an emphasis in Aeroacoustics. He accepted a graduate research assistantship with the Aeroacoustics group at the National Center for Physical Acoustics at the University of Mississippi, where he worked under Dr. Nathan Murray. He also joined the ROTC program, and was honored as a Distinguished Military Graduate upon completing it. During his time at the University of Mississippi, Farrell maintained a 3.6 GPA and was elected once to the General Student Body Government and twice the Graduate Student Body Government. Farrell assessed with the Army National Guard as an Aviation Officer and received his commission as a Second Lieutenant in December 2011.